# Effects of early marine diagenesis and site-specific depositional controls on carbonate-associated sulfate: insights from paired S and O isotopic analyses

Jocelyn A. Richardson[1*], Aivo Lepland[2,3], Olle Hints[3], Anthony R. Prave[4], William P. Gilhooly III[5], Alexander S. Bradley[1] and David A. Fike[1*]

[1]Department of Earth and Planetary Sciences, Washington University, St. Louis, MO 63130 USA

[2]Geological Survey of Norway, 7491 Trondheim, Norway

[3]Department of Geology, Tallinn University of Technology, Ehitajate 5, 19086 Tallinn, Estonia

[4]School of Earth and Environmental Sciences, University of St Andrews, Fife, KY16 9AL, Scotland

[5] Department of Earth Sciences, Indiana University-Purdue University Indianapolis, Indianapolis, IN, USA

*Corresponding authors:

E-mail: jocelynr@slac.stanford.edu. Phone: +1 (650) 926-5145

E-mail: dfike@levee.wustl.edu. Phone: +1 (314) 935-6607

Keywords: carbonate-associated sulfate, CAS, sulfur isotopes, sulfate oxygen isotopes, Ireviken bioevent, Silurian

19  **Abstract**

20  Carbon, sulfur and oxygen isotope profiles in Silurian strata of the Baltoscandian Basin (Estonia),

21  coincident with the Ireviken Bioevent, provide insights into basin-scale and platform-specific

22  depositional processes. Paired carbon isotope records preserve a positive isotope excursion during

23  the early Wenlock, coincident with faunal turnover, yet $\delta^{13}C$ variability of this excursion compared

24  to other locations within the paleobasin reflects local depositional influences superimposed on a

25  global signal. In comparison, sulfur isotope records do not preserve a systematic isotopic excursion

26  over the same interval. Instead, sulfur isotope records have high sample-to-sample stratigraphic

27  variability, particularly in shallow-water carbonate rocks (scatter up to ~10‰ for $\delta^{34}S_{CAS}$ and

28  ~25‰ for $\delta^{34}S_{pyr}$). This pattern of isotopic variability is also found between sites from the same

29  carbonate platform, where the magnitude and isotopic variability in $\delta^{34}S_{CAS}$ and $\delta^{34}S_{pyr}$ differ

30  depending on relative local sea level (and therefore facies). Such facies-dependent variability

31  reflects more closed- versus more open-system diagenetic conditions where pulses of increased

32  sedimentation rate in the shallow water environments generates greater isotopic variability in both

33  $\delta^{34}S_{CAS}$ and $\delta^{34}S_{pyr}$. Increased reworking and proximity to the shoreline results in local sulfide

34  oxidation, seen as a decrease in $\delta^{34}S_{CAS}$ in the most proximal settings. Platform-scale evolution of

35  isotopically distilled pore-fluids associated with dolomitization results in increased $\delta^{34}S_{CAS}$ in deep

36  water settings. Correlations in paired $\delta^{34}S_{CAS}$-$\delta^{18}O_{CAS}$ data support these conclusions,

37  demonstrating the local alteration of CAS during deposition and early marine diagenesis. We

38  present a framework to assess the sequence of diagenetic and depositional environmental processes

39  that have altered $\delta^{34}S_{CAS}$ and find that $\delta^{34}S$ of ~27-28‰ approximates Silurian seawater sulfate.

40  Our findings provide a mechanism to understand the elevated variability in many deep-time

41  $\delta^{34}S_{CAS}$ records that cannot otherwise be reconciled with behavior of the marine sulfate reservoir.

## 1.0 Introduction

The evolution of global biogeochemical cycles over Earth history is recorded in the chemical abundances and isotopic ratios of elements in marine sedimentary rocks (e.g. Bartley and Kah, 2004; Garrels and Lerman, 1981). The isotopic ratios of carbon and sulfur are particularly informative because values from both oxidized and reduced phases (carbonate, organic carbon, sulfate, sulfide) are preserved, and can be measured, in carbonate rocks. Changes in these isotopic ratios over time are typically inferred to represent perturbations to the carbon and sulfur cycles; efforts to understand the source of these perturbations have recognized the importance of deconvolving global versus local processes (Fike et al., 2015; Jones et al., 2019; Pasquier et al., 2017; Rose et al., 2019).

Variations in carbon isotope values ($\delta^{13}C$) of carbonate and organic carbon through time can be attributed to global carbon cycle perturbations (Kump and Arthur, 1999) and/or local processes, such as: facies changes (e.g. Rose et al., 2019), variations in productivity between deep- and shallow-marine settings and its effect on the dissolved inorganic carbon (DIC) pool (e.g. Jones et al., 2019; Swart and Eberli, 2005), changes in carbonate mineralogy, and sediment- versus fluid-buffered diagenesis (Higgins et al., 2018). Moreover, the stratigraphic expression of carbon isotope excursions can be variable in magnitude and duration between time-correlative sections (Jones et al., 2019; Samtleben et al., 2000), complicating efforts to understand the mechanism generating the $\delta^{13}C_{carb}$ signals.

Sulfur archives in the sedimentary record include oxidized sulfur in gypsum, anhydrite, barite (Paytan, 1998; Strauss, 1997) and carbonate-associated sulfate (CAS) (Burdett et al., 1989), as well as reduced sulfur sinks in pyrite and organic S compounds (Canfield, 2001). Microbial

65  sulfate reduction (MSR) can impart an isotopic fractionation that leaves the resultant product

66  sulfide depleted in $^{34}$S relative to the sulfate pool by as much as 70‰ (Eldridge et al., 2016; Sim

67  et al., 2011). Due to the spatial and temporal extent of carbonate strata and their ability to preserve

68  sulfur isotope ($\delta^{34}$S) records of both CAS and pyrite, carbonate rocks have been investigated to

69  constrain the evolution of the global sulfur cycle.

70      Stratigraphic datasets of coeval pyrite and CAS $\delta^{34}$S have traditionally been interpreted to

71  record changes to the global sulfur cycle, reflecting one or a combination of: changes to the burial

72  and weathering fluxes of pyrite and/or sulfate minerals, the size of the marine sulfate reservoir,

73  and/or the dominant microbial metabolic community and the associated biological fractionation

74  (Canfield, 2001; Garrels and Lerman, 1981). Recent studies aiming to reconstruct the ancient

75  sulfur cycle have generated highly variable, both regionally and stratigraphically, sulfur isotope

76  datasets in $\delta^{34}$S$_{pyr}$ and $\delta^{34}$S$_{CAS}$ (Jones and Fike, 2013; Thompson and Kah, 2012; Young et al.,

77  2016). Such large, commonly facies-dependent, variability in $\delta^{34}$S$_{pyr}$ (e.g. Richardson et al., 2019a;

78  Rose et al., 2019), is not unexpected as pyrite typically forms within sediments under evolving

79  diagenetic conditions. Moreover, there is a good framework in place to understand such variability

80  in terms of local environmental parameters, such as sedimentation rate and/or organic carbon

81  loading (Aller et al., 2010; Bryant et al., 2019; Claypool, 2004; Fike et al., 2015; Liu et al., 2019;

82  Pasquier et al., 2017). Yet the origin and environmental significance of variability in $\delta^{34}$S$_{CAS}$, often

83  interpreted to record global marine sulfate, remains poorly understood. Typical sample-to-sample

84  bulk rock $\delta^{34}$S$_{CAS}$ can vary as much as 10-12‰ within an individual stratigraphic section, which

85  is difficult to reconcile with the behavior of the marine sulfate reservoir unless the concentration

86  of seawater sulfate was very low (Fike et al., 2015). Interpretations of the source of this 'noise'

87  include basin- to global-scale sulfur cycle perturbations (Adams et al., 2010; Gill et al., 2007;

88    Kozik et al., 2019; Stebbins et al., 2018; Thompson and Kah, 2012) and locally variable

89    depositional and early diagenetic environments (Present et al., 2019; Richardson et al., 2019a;

90    Rose et al., 2019). To better understand the origin of this variability in $\delta^{34}S_{CAS}$, we seek additional

91    information by measuring the oxygen isotopic composition in CAS.

92         Oxygen isotope values of sulfate ($\delta^{18}O_{SO4}$) are a supplementary proxy to interrogate the

93    operation of the sulfur cycle. At normal seawater temperatures and pH, oxygen isotopes between

94    sulfate and seawater require $10^{6-7}$ years to abiotically equilibrate (Chiba and Sakai, 1985). In the

95    absence of diagenetic alteration and overprinting, $\delta^{18}O_{SO4}$ variability over longer geologic

96    timescales will reflect changes in the major fluxes involving sulfate in the sulfur cycle, and $\delta^{18}O_{SO4}$

97    variability over shorter geologic timescales ($< 10^6$ years) reflects the dominant metabolisms within

98    local microbial sulfur cycling (MSR, sulfide oxidation, sulfur disproportionation) and/or abiotic

99    sulfide and pyrite oxidation (Bottrell and Newton, 2006; Turchyn and Schrag, 2006). Holding all

100   other variables constant, MSR will result in an increase in paired $\delta^{34}S_{SO4}$-$\delta^{18}O_{SO4}$ values, while

101   sulfide oxidation will be tracked as a coeval decrease in paired $\delta^{34}S_{SO4}$-$\delta^{18}O_{SO4}$ data (Goldberg et

102   al., 2005). A decoupling of $\delta^{34}S_{SO4}$-$\delta^{18}O_{SO4}$ is generally understood to reflect differences in global

103   vs. local influence on these isotope systems (Turchyn and Schrag, 2006). Consequently, paired

104   $\delta^{34}S_{SO4}$-$\delta^{18}O_{SO4}$ and $\delta^{34}S_{SO4}$-$\delta^{34}S_{pyr}$ can be powerful tools for reconstructing the global and local

105   sulfur cycles in ancient carbonate successions (Rennie and Turchyn, 2014).

106        We used the well-characterized Silurian stratigraphy of the East Baltic portion of the

107   Baltoscandian Basin (e.g. Cramer et al., 2010; Hints et al., 2006; Kaljo and Martma, 2000; Kiipli

108   et al., 2006, 2008; Loydell et al., 2010; Rose et al., 2019; Samtleben et al., 2000; Young et al.,

109   2020) and $\delta^{13}C_{carb}$, $\delta^{13}C_{org}$, $\delta^{34}S_{CAS}$, $\delta^{34}S_{pyr}$ and $\delta^{18}O_{CAS}$ data for reconstructing the potential

110   controls on these proxies during a period of rapid environmental change (Munnecke et al., 2010,

111    2003). The Baltoscandian Basin preserves an abundance of relatively continuous outcrop and drill

112    core sections spanning the late Ordovician through Silurian, providing a platform to assess the

113    causes and consequences of some of the earliest extinction events in the Phanerozoic. One such

114    extinction event, known as the Ireviken bioevent (IBE; Calner, 2008; Jeppsson, 1997; Munnecke

115    et al., 2003; Tonarová et al., 2014) occurs at the Llandovery-Wenlock boundary, associated with

116    a globally documented carbon isotope excursion and paleoclimate perturbations (Lehnert et al.,

117    2010; Trotter et al., 2016). Additionally, the short duration of the stages in the Silurian (e.g. Cramer

118    et al., 2010), combined with the number of time-correlative stratigraphic sections in the

119    Baltoscandian Basin, serves as a framework to evaluate whether the observed geochemical

120    perturbations result from global environmental phenomena. We present new $\delta^{13}C_{carb}$, $\delta^{13}C_{org}$,

121    $\delta^{34}S_{CAS}$, $\delta^{34}S_{pyr}$ and $\delta^{18}O_{CAS}$ data from the Silurian strata in the upper 112 m of the Paatsalu drill

122    core, Estonia. This interval is temporally correlative with strata in the Viki core, Estonia

123    (Richardson et al., 2019a), and in Gotland, Sweden (Rose et al., 2019), which together provide a

124    basin-wide transect of early Silurian sedimentary strata.

125

126    **2.0 Geological Setting**

127    The studied Paatsalu drill core from western Estonia (Fig. 1; 58°5' N 23°7'E) spans from the mid-

128    Llandovery to the mid-Wenlock (ca 440 to 432 Ma). The section represents the northern margin

129    of the Baltoscandian Basin, an early Paleozoic epicontinental sea on Baltica and then Laurussia

130    (Baarli et al., 2003; Cocks and Torsvik, 2005; Nestor and Einasto, 1997). During the early Silurian,

131    the region was located at tropical southern latitudes (Torsvik and Cocks, 2013). Various warm-

132    water carbonates and marly deposits accumulated in the shallow part of the basin, such as in central

133    Estonia. Deeper shelf facies, characterized by the deposition of organic-rich muds, were located

134     towards the south and west from the study site (Fig. 1; Nestor & Einasto, 1997; Baarli et al., 2003).

135     The stratigraphic framework of the Silurian of the Paatsalu core is based largely on chitinozoan

136     and conodont biostratigraphy (Hints et al., 2006; Rubel et al., 2007) and K-bentonites (Kiipli et

137     al., 2006, 2008). Additionally, carbon isotope chemostratigraphy can be applied and numerous

138     reference sections from the region can be used for comparison (Kaljo and Martma, 2006, 2000).

139     Five formations are identified through this interval in the Paatsalu drill core: the Nurmekund,

140     Rumba, Velise, Jaani and Muhu formations.

141         The lowermost Nurmekund Formation (111.8 m depth), which correlates to the late-

142     Rhuddanian and Aeronian (Kaljo and Martma, 2000), consists of interbedded carbonate mudstone

143     and grainstone with varying abundances of bioclastic material deposited within lagoonal

144     (mudstone) and shoreline (grainstone) environments. The base of the Rumba Formation (102–83

145     m) is marked by a 2-m-thick, sharp-based, low-angle cross-bedded grainstone overlain by

146     interbedded wackestones and packstones with echinoderms, brachiopods and bryozoans, with a

147     small abundance of interbedded mudstone. These facies indicate deposition within inner-shelf, reef

148     and shoal settings. A 20-cm-thick bentonite bed at 88 m depth is correlative with one at 185.1 m

149     depth in the Viki core (Kiipli et al., 2006). The overlying Velise Formation (83–70 m depth) is

150     composed of grey-green siliciclastic mudstone and marlstone with abundant pyrite in the form of

151     small aggregates, large euhedral crystals and pyritized burrows and echinoderm fragments; these

152     facies represent a mid- to outer-shelf setting. Partial dolomitization of the carbonates begins in the

153     middle of the Velise Formation through to the top of the core. An erosive-based 1-m-thick oolitic

154     packstone at 70.5 m marks the base of the Jaani Formation (70–34 m depth), defining a sequence

155     boundary placing inner-shelf facies (the oolite) on top of mid-outer shelf marlstones (Velise

156     Formation). Above this, the Jaani Formation consists of dolomitized grey-green mud-marlstones

157 like those in the Velise Formation. Macroscopic pyrite is visible within the first meter of the

158 marlstone, but size and abundance decrease upwards. The marlstone grades into bioclastic, nodular

159 micritic limestone, reflecting a progressive shallowing into mid-shelf settings. The Muhu

160 Formation (34 m depth to top of the core) consists of interbedded bioclastic (echinoderms,

161 brachiopods, bryozoans) wackestone and packstone in the lower 11 m, with an increasing

162 abundance of mud drapes upward into thinly interbedded dolomitic arenite with dolomitized

163 mudstone and wackestone at the top of the core. Overall, the succession records two large-scale

164 depositional cycles. The Nurmekund formation represents the upper part of the "Early-Middle

165 Llandovery macrocycle" (Nestor & Einasto, 1997); it is followed by a regional hiatus and

166 denudation during the late Aeronian. The "Late Llandovery - Middle Wenlock macrocycle" is

167 represented by a full transgressive-regressive cycle in the Paatsalu core: a gradual deepening to

168 inner-mid shelf settings (Rumba Formation) and even deeper mid-outer shelf facies (Velise

169 Formation) during the Telychian; then a sequence boundary that coincides with a gap (Männik et

170 al., 2014) and marks a return to inner-mid shelf settings (oolite at the base of the Jaani Formation)

171 with a subsequent flooding surface to outer-shelf facies (Jaani Formation) and then shallowing into

172 peritidal environments (Muhu Formation). As a result of the early-mid Wenlock regression the

173 basin transformed into a more restricted gulf-like pericratonic sea (Nestor & Einasto, 1997).

174

175 **3.0 Methods**

176 The Paatsalu drill core material is housed at the Särghaua core repository, Tallinn University of

177 Technology (https://geocollections.info/drillcore/128). A total of 62 samples from the Paatsalu

178 core were collected, cut, crushed and powdered in a Spex 8515 Shatterbox. Homogenized powders

179 were divided for each type of analysis. Carbon and sulfur isotope analyses, together with elemental

180     abundance analyses, were carried out at Washington University in St. Louis, USA. Analyses for

181     oxygen isotopes of CAS were performed in the analytical facilities at Indiana University-Purdue

182     University Indianapolis, USA.

183         For carbonate carbon and carbonate oxygen isotope analyses, ~100 µg of sample powder

184     was dissolved in 100% phosphoric acid ($H_3PO_4$) for at least 4 hours at 70°C (accounting for

185     differences in acid digestion of calcite-dolomite mixtures; Xi Liu et al., 2019). Sample vials were

186     flushed with He and the evolved $CO_2$ was measured on a Thermo Finnigan Gasbench II coupled

187     to a Delta V Advantage Isotope Ratio Mass Spectrometer. Organic carbon isotope analyses were

188     performed on the organic residue left after decarbonating 4–5 g of sample powder with 6M HCl.

189     Acidifications were left for up to 20 minutes and were repeated until there was no visible reaction

190     when HCl was added. Insoluble residues were analyzed for organic carbon isotope composition

191     on a Flash 2000 Organic Elemental Analyzer coupled via a ConFlo IV to a Delta V Plus Isotope

192     Ratio Mass Spectrometer. Carbon and oxygen isotopes are expressed in standard delta notation

193     ($\delta^{13}C$, $\delta^{18}O$) in permil (‰) relative to the Vienna Pee Dee Belemnite (VPDB) standard with 1 σ

194     error on $\delta^{13}C_{carb}$, $\delta^{18}O_{carb}$ and $\delta^{13}C_{org}$ of 0.15‰ based on standard and replicate samples.

195         Preparation of samples for analysis of sulfur and oxygen isotopic ratios in CAS and for

196     analysis of sulfur isotopic ratios of pyrite followed Richardson et al. (2019a). Sample powder (30–

197     50 g) was soaked in a 10% brine (NaCl) solution for 30 minutes and then decanted. This step aimed

198     to remove any free sulfur species that might be adsorbed onto the carbonate. After a total of three

199     brine rinses, the supernatant was checked for sulfate by adding 1 ml of saturated $BaCl_2$ solution

200     and additional brine rinses were performed if any precipitate formed in the supernatant. This was

201     followed by 3 rinses with deionized $H_2O$. Samples were acidified with 6M HCl and stirred for up

202     to 3 hours (or until there was no visible reaction) to release CAS. The acidic supernatant was

203    filtered and reacted with an excess of $BaCl_2$ to precipitate $BaSO_4$ which was rinsed, weighed and

204    dried for analyses. To extract pyrite as chromium-reducible sulfur (Canfield et al., 1986), insoluble

205    residues from the CAS extraction were reacted with a 6M HCl and 2M chromium (II) chloride

206    solution under constant $N_2$ gas and were left stirring for 4 hours just below the boiling point. The

207    evolved gas from the sample reaction was passed through a water trap and bubbled into a test tube

208    containing silver nitrate solution in deionized $H_2O$ in order to precipitate silver sulfide.

209        Sulfur isotope analyses were performed by combining ~350 µg of silver sulfide or barium

210    sulfate with 1–3 mg of vanadium pentoxide and converted to $SO_2$ using a Costech ECS 4010

211    elemental analyzer coupled to a Thermo Finnigan Delta V Plus mass spectrometer. Separate

212    aliquots of 150 µg barium sulfate (from both the Paatsalu and Viki core) were combined with an

213    equal amount of graphite in a silver capsule then loaded into a nitrogen-purged Costech Zero-blank

214    autosampler and analyzed for oxygen isotopes by pyrolysis (at 1450ºC) using a Thermo TC/EA

215    coupled to a Thermo Delta V Plus mass spectrometer. Sulfur isotope values are expressed in

216    standard delta notation ($\delta^{34}S$) in permil (‰) as a deviation from the Vienna Canyon Diablo Troilite

217    (VCDT) standard and have a 1σ error of 0.3‰ and 0.2‰ for $\delta^{34}S_{CAS}$ and $\delta^{34}S_{pyr}$ respectively. The

218    oxygen isotope composition of sulfate is reported in delta notation ($\delta^{18}O$) relative to Vienna

219    Standard Mean Ocean Water (VSMOW), where the 1σ error on $\delta^{18}O_{CAS}$ is 0.2‰, based on

220    standards and replicate samples.

221        Elemental abundance within the carbonate fraction of rock powders were prepared

222    following the protocol of Husson et al., (2015). Data were collected using a PerkinElmer Optima

223    7300DV ICP-OES and standardized to the Sigma Multi-element Standard Solution 5. Abundances

224    are given in ppm.

225

226 **4.0 Results**

227 *4.1 Carbon Isotopes*

228 The strata from the Paatsalu core preserve a smoothly varying $\delta^{13}C_{carb}$ record (Fig. 2). In the

229 Nurmekund Formation, $\delta^{13}C_{carb}$ increases from 0‰ to 1.3‰ between 111.8 and 108.5 m depth

230 before declining to -1.3‰ at 98.2 m depth in the lower Rumba Formation ('Rumba low'; Kaljo

231 and Martma, 2000). Values increase to 0.4‰ at 86.2 m depth and jump to 2‰ at 83.4 m depth

232 (over a discontinuity in sampling) near the top of the Rumba Formation and remain near 2‰

233 through the Velise Formation. Between 70 and 66 m depth, in the oolitic packstone at the base of

234 the Jaani Formation, $\delta^{13}C_{carb}$ values increase to 4‰, reaching a maximum of 4.8‰ at 51 m depth

235 and from there decrease steadily through the Muhu Formation to around -0.4‰ at the top of the

236 core. The positive $\delta^{13}C_{carb}$ excursion to 4.8‰ is approximately time-correlative to the IBE recorded

237 in numerous sections worldwide (Hints et al., 2006; Munnecke et al., 2003; Richardson et al.,

238 2019a; Rose et al., 2019).

239 The base of the Nurmekund Formation is marked by $\delta^{13}C_{org}$ values of -29‰ that decrease

240 to -31.2‰ in the lower part of the formation (Fig. 2). $\delta^{13}C_{org}$ then increases through the Rumba

241 and Velise formations to -27.2‰ at 70 m depth and continues to increase to -24.7‰ at 68.6 m

242 depth across the base of the Jaani Formation. Above this, there is a small decline to -26.9‰ at 38

243 m depth, but values increase to -25.7‰ at the top of the Formation. Notably, from c. 60 to 35 m

244 depth $\delta^{13}C_{org}$ and $\delta^{13}C_{carb}$ show opposite trends. From 36 to 16.5 m depths $\delta^{13}C_{org}$ varies, between

245 -26‰ and -24‰ before decreasing to -30‰ toward the top of the core.

246

247 *4.2 Sulfur Isotopes*

248    The Paatsalu $\delta^{34}S_{CAS}$ data have typical sample-to-sample variability of 1–4‰ and maximal

249    sample-to-sample variability of 7–10‰ (Fig. 2; Table 1). The lowermost samples in the

250    Nurmekund Formation decrease from 33‰ to 23.4‰ into the basal Rumba Formation. Values

251    become more variable, ranging between 29.7‰ and 17.5‰, through to the top of the Rumba

252    Formation at 84.3 m depth. In the Velise Formation, $\delta^{34}S_{CAS}$ values are more positive and less

253    variable between 25.4‰ and 32‰. In the Jaani Formation, $\delta^{34}S_{CAS}$ values are tightly clustered

254    around 27.5‰ (except one sample, 15‰, at 67.2 m depth) up to 46.2 m depth. Above this, values

255    decrease into the Muhu Formation, reaching 15.6‰ at 20 m depth. From 20 m depth to the top of

256    the core, $\delta^{34}S_{CAS}$ values vary between 3.3‰ and 14‰ to the top of the core. Overall, three main

257    trends are observed: (i) variable $\delta^{34}S_{CAS}$ (sample-to-sample variability as much as 5.5‰) in the

258    Nurmekund and Rumba formations; (ii) relatively invariant $\delta^{34}S_{CAS}$ between 25 and 30‰ in the

259    Velise and Jaani formations; and (iii) declining $\delta^{34}S_{CAS}$ in the Muhu Formation, becoming

260    increasingly variable toward the top of the core.

261        Sulfur isotope values in pyrite range from 1‰ to 15.4‰ in the lower 10 m of the studied

262    section (Fig. 2; Table 1). Above 102.5 m depth, $\delta^{34}S_{pyr}$ decreases from 10.9‰ to -21.8‰ over 4

263    m. Between 98.2 m and 80.3 m depth (the Rumba Formation), $\delta^{34}S_{pyr}$ varies between -20‰ and -

264    30‰ with one outlier (2.8‰) at 83.4 m depth. At 78 m, $\delta^{34}S_{pyr}$ increases to 4.6‰ and continues to

265    increase through the Velise Formation up to 15.4‰, except for one sample (-32.3‰) at 74.24 m.

266    At the base of the Jaani Formation values decrease to -14.3‰ and continue to decrease to -21.1‰

267    at 62.9 m depth. Above that, $\delta^{34}S_{pyr}$ increases to c. -2‰ at 35 m depth, stabilizes around -9‰ from

268    32.5 to 16.5 m depth and then decreases to -14.5‰ to the top of the core. In summary, the

269    Nurmekund and Velise formations have highly variable $\delta^{34}S_{pyr}$ values, while the Jaani and Muhu

270 Formations exhibit intermediate and moderately variable $\delta^{34}S_{pyr}$ (with increasing variability in

271 $\delta^{34}S_{pyr}$ up-section), and the Rumba Formation has the least $\delta^{34}S_{pyr}$ variability.

| Table 1. Sulfur isotope variability for the Paatsalu core | | | | | |
|---|---|---|---|---|---|
| Formation (n = samples) | Facies | average $\delta^{34}S_{CAS}$ | avg sample-to-sample $\delta^{34}S_{CAS}$ difference | average $\delta^{34}S_{pyr}$ | avg sample-to-sample $\delta^{34}S_{pyr}$ difference |
| Nurmekund (4) | shoreline-lagoon | 28.9 | 3.2 | 8.5 | 8.9 |
| Rumba (14) | inner-mid shelf | 24.8 | 3.3 | -19.9 | 4.5 |
| Velise (9) | mid-outer shelf | 29.3 | 2.6 | -7.6 | 16.4 (8.3) |
| Jaani (30) | outer shelf | 27.2 | 2.4 | -9.6 | 7.0 (4.2) |
| Muhu (12) | shoreline | 14.5 | 5.1 | -9.8 | 5.7 |

272 *4.3 Oxygen Isotopes*

273 The $\delta^{18}O_{carb}$ values in the Nurmekund Formation decrease from -5.2‰ to -6.7‰ at 102.6

274 m. In the Rumba and lower Velise formations, values remain around -6‰ to ~71.5 m depth and

275 become increasingly variable up to 59 m depth in the lower Jaani Formation. Values converge

276 around -6‰ at 39.3 m depth and variability decreases. There is a step increase in $\delta^{18}O_{carb}$ values

277 from -5.5‰ to -2‰ around 39 m depth, with values stabilizing around -4‰ through to the top of

278 the core. In general, $\delta^{18}O_{carb}$ values are relatively invariant, between -5‰ and -7‰, in the

279 Nurmekund Formation through the base of the Muhu Formation (111.8 to 39.3 m depth; Fig. 2).

280 $\delta^{18}O_{carb}$ values are higher and more variable between -2‰ and -4.5‰ from 39 m to the top of the

281 core.

282 The oxygen isotope values of CAS have similar stratigraphic variability and trends as

283 $\delta^{34}S_{CAS}$ (Fig. 2). At the base of the Paatsalu section, $\delta^{18}O_{CAS}$ is 12.4‰ and decreases to 10.6‰ at

284 105.3 m depth. Values increase variably from 10‰ to 15.6‰ at the top of the Velise Formation at

285 71.5 m depth. In the Jaani Formation (67.2 m depth), $\delta^{18}O_{CAS}$ decreases to 8.3‰ before increasing

286 to 14.5‰ at 63 m depth and then remains relatively invariant. From 42 to 26.9 m depth, $\delta^{18}O_{CAS}$

287 becomes increasingly variable (between 11.5‰ and 15‰ with one outlier of 20.3‰ at 36 m depth),

288 and then decreases through the Muhu Formation, reaching the lowest $\delta^{18}O_{CAS}$ value in the core (-

289 1.2‰ at 9.6 m depth).

290 To complement these data from the Paatsalu core, we also present new $\delta^{18}O_{CAS}$ data from

291 the previously studied Viki core (Fig. 3). The base of the Viki core begins in the Varbola Formation

292 (see Richardson et al., 2019a) at 240.6 m depth with $\delta^{18}O_{CAS}$ of 17.9‰, which decreases

293 throughout the Varbola Formation to approximately 15‰ at 228.5 m depth. $\delta^{18}O_{CAS}$ is variable

294 between 11.5 and 17.4‰ through the upper Varbola and lower Nurmekund formations. At 208.4

295 m, $\delta^{18}O_{CAS}$ increases from 12.4 to 16.5‰ at 180 m depth in the lowermost Velise Formation. From

296 168.3 – 107.4 m depth, values are variable around 15‰ throughout the Velise and lower Jaani

297 formations. Above this, $\delta^{18}O_{CAS}$ increases to 20‰ at 97.7 m depth before returning to 15‰ at 87.6

298 m depth in the upper Jaani Formation. From 87.6 m to the top of the section, $\delta^{18}O_{CAS}$ values

299 increase to 17.4‰.

300

301 **5.0 Discussion**

302 Carbon, sulfur and oxygen isotopic ratios in carbonate successions have been used to track the

303 operation and evolution of global biogeochemical cycles through geologic time (Canfield, 2001;

304 Kump and Arthur, 1999). However, frequency, magnitude and duration of isotopic changes can

305 also result from basin-specific processes, depositional controls, diagenesis, or combinations of

306 these processes. Therefore, the nature of isotope excursions must be independently assessed in any

307 given succession. Within the Paatsalu core, carbon isotopic ratios in carbonate and organic matter

308    generally co-vary, whereas sulfur isotopic records of $\delta^{34}S_{CAS}$ and $\delta^{34}S_{pyr}$ do not. Additionally, the

309    variability in $\delta^{34}S_{CAS}$, $\delta^{18}O_{CAS}$ and $\delta^{34}S_{pyr}$ (Table 1) commonly occurs too rapidly (with respect to

310    the residence time of seawater sulfate) for this variability to reflect global perturbations to the

311    seawater sulfate reservoir via canonical, global-scale mechanisms. Fluid inclusion data from the

312    Silurian shows seawater sulfate concentrations from 5-12 mM (Lowenstein et al., 2003),

313    approximately 17-43% of the modern ocean value. The residence time of a reservoir is the ratio of

314    the size of the reservoir to the input or output flux; estimates for modern seawater sulfate residence

315    times range from 13-20 Ma (Canfield 2004; Bottrell and Newton, 2006). Based on conodont

316    biostratigraphy, this 112 m section of the Paatsalu core records < 15 Myr (Figs. 2 and 3), and the

317    carbon isotope excursion (coincident with the IBE) lasts ~1 Myr (Cramer et al., 2011). In addition,

318    the size of the modern ocean sulfate reservoir buffers $\delta^{34}S_{SO4}$ to a maximum rate of change of

319    0.5‰ per Myr (Kah et al., 2004). Here, an average rate of change for $\delta^{34}S_{CAS}$ of 1.3‰ per Myr

320    would require seawater sulfate concentrations to be < 4.5 mM for this rate of change to be

321    consistent with the size of the expected marine sulfate reservoir (Kah et al., 2004). Thus, marine

322    sulfate should have relatively invariant $\delta^{34}S_{SO4}$ and $\delta^{18}O_{SO4}$ values over the timescale of the

323    individual formations recovered in the Paatsalu core. As noted above, variability in $\delta^{34}S_{CAS}$,

324    $\delta^{18}O_{CAS}$ and $\delta^{34}S_{pyr}$ show high sample-to-sample variability, which we consider to be far too rapid

325    to reflect worldwide perturbations to the global sulfur cycle.

326

327    *5.1 Diagenesis*

328    For reliable interpretation of the evolution of local or global biogeochemical cycles as recorded by

329    geochemical signatures, it is essential to assess diagenetic alteration of carbonate proxies by fluid

330    migration, carbonate recrystallization, or dolomitization during early or late marine diagenesis, or

331  by non-marine fluids during burial or meteoric diagenesis (e.g. Banner and Hanson, 1990;

332  Halverson et al., 2007; Marenco et al., 2008b). Carbonate diagenesis is complex and can impact

333  mineralogy, lithofacies and different portions of carbonate platforms heterogeneously.

334  Consequently, there are a number screening tools used to interpret the extent of diagenetic

335  alteration of the geochemical signals that are of interest to our understanding of past Earth

336  environments (Swart, 2015). To assess the *most likely* alteration mechanisms influencing sulfur

337  isotope signals (values and variability) and to determine the *least altered* $\delta^{34}S_{CAS}$ values we used:

338  (1) elemental analyses and isotope relationships as a coarse indicator for determining the type of

339  fluid-rock interaction; (2) $\delta^{34}S_{CAS}$ and abundance relationships to assess direct influences on

340  $\delta^{34}S_{CAS}$; (3) evaluation of geochemical data within a lithologic context; and (4) assessment of

341  $\delta^{34}S_{CAS}$ and $\delta^{18}O_{CAS}$ relationships to understand inherent early marine diagenetic processes.

342

343  *5.1.1 Post-depositional fluid-rock interactions*

344  Common indicators of diagenesis, such as Sr abundance and correlations between Mn vs.

345  Sr, Fe vs. Sr and $\delta^{13}C_{carb}$ vs. $\delta^{18}O_{carb}$, are generally used to screen samples for evidence of meteoric,

346  burial, brine and marine diagenesis (Banner and Hanson, 1990; Bartley et al., 2001; Erhardt et al.,

347  2020; Halverson et al., 2007; Turchyn et al., 2009). Sr abundance is considered an approximate

348  indication of the degree of carbonate recrystallization, as most fluids distinct from seawater will

349  remove Sr from carbonate minerals with progressive recrystallization. In this study all samples

350  have Sr abundance < 200 ppm (Fig. 4) which is much lower than typical 'primary' carbonate (often

351  > 1000 ppm). Thus the entire succession has likely experienced some degree of alteration and we

352  do not consider stratigraphic changes in Sr abundance a clear indicator for the type of fluid

353  interaction in these samples (Ahm et al., 2018; Halverson et al., 2007).

354        Although Mn, Sr and Fe relationships were initially understood to reflect varying degrees

355    of meteoric diagenesis (Brand and Veizer, 1980), Mn, Sr and Fe correlations can also help evaluate

356    the degree of fluid interactions under anoxic conditions (e.g. Turchyn et al., 2009). Our data show

357    increases in Mn and Fe with concurrent decreases in Sr, possibly indicating meteoric diagenesis

358    or progressive carbonate recrystallization under anoxic conditions (Figs 4A-B). Lime mudstone,

359    wackestone, and packstone facies from the Nurmekund and Rumba Formations have the highest

360    Sr and lowest Mn and Fe abundances, suggesting that these facies are the least diagenetically

361    altered, though not necessarily primary (Fig. 4A). In contrast, $\delta^{13}C_{carb}$ vs. $\delta^{18}O_{carb}$ do not covary

362    (Fig. 4C), even those samples from outside the positive $\delta^{13}C_{carb}$ excursion, in a manner consistent

363    with alteration by meteoric or burial (brine) fluids (Banner and Hanson, 1990), where meteoric

364    fluids are depleted in both $^{13}C$ and $^{18}O$ while brine fluids are commonly depleted in $^{18}O$ relative to

365    seawater (Swart, 2015). In addition, the small offset between $\delta^{18}O_{carb}$ presented here and $\delta^{18}O_{carb}$

366    values from similarly aged, well-preserved brachiopods (-4.5 to -5.5‰; Azmy et al., 1998),

367    suggests that $\delta^{18}O_{carb}$ in the Paatsalu section has been affected by seawater-like diagenetic fluids,

368    perhaps under anoxic conditions. Despite this, we find no correlation between $\delta^{18}O_{carb}$ and any

369    other geochemical parameter measured. Together, this indicates correlations between Mn, Fe and

370    Sr are most likely due to fluid interactions under anoxic conditions.

371        To assess alteration associated with dolomitization, lithology-specific $\delta^{34}S_{CAS}$ is plotted

372    against Mg/Ca ratio (Fig. 5A) (Marenco et al., 2008b). Samples with Mg/Ca ratio < 0.125 have

373    $\delta^{34}S_{CAS}$ values between 21‰ and 33‰, which is not uncommon for unaltered marine carbonates

374    of this age (Present et al., 2020) and is similar to those in the nearby Viki core (Richardson et al.,

375    2019a). At higher Mg/Ca ratios (> 0.35), $\delta^{34}S_{CAS}$ values span the entire range observed in the

376    Paatsalu core. The large range of $\delta^{34}S_{CAS}$ in the dolomitized samples could indicate distinct

377     dolomitizing processes that give rise to both increased and decreased $\delta^{34}S_{CAS}$ values. Partial

378     dolomitization is present from 75 m to the top of the Paatsalu core (from the top of the Velise

379     through the Muhu Formation). The $\delta^{34}S_{CAS}$ of dolomitized samples from the upper Velise and

380     Jaani Formation are relatively stable (varying between ~ 25‰ and 30‰) and are similar to the

381     $\delta^{34}S_{CAS}$ values from unaltered marlstone of the lower Velise Formation (Fig. 5). This implies that

382     the dolomitizing fluids did not overprint $\delta^{34}S_{CAS}$ from the upper Velise and Jaani Formation, such

383     that the composition of the dolomitizing fluid was not appreciably offset from seawater.

384     Comparatively, the Muhu Formation has the least variable and highest Mg/Ca ratios and also

385     records the lowest $\delta^{34}S_{CAS}$ values (3-25‰). In this case, the composition of the dolomitizing fluid

386     progressively evolved with sulfate sourced from sulfide oxidation, decreasing $\delta^{34}S_{CAS}$ values in

387     the recrystallizing carbonate. The dolomitizing fluid was the most evolved during dolomitization

388     of the uppermost Muhu Formation, where $\delta^{34}S_{CAS}$ values are particularly low (3-15‰). It has been

389     shown that enhanced evaporation and MSR can encourage dolomitization (Baldermann et al.,

390     2015; Fichtner et al., 2017), and such dolomitization has been shown to incorporate isotopically

391     light [34]S-sulfate, particularly in near shore environments (e.g. Fichtner et al., 2017; Marenco et al.,

392     2008b; Present et al., 2015). This process may have had an additional impact on the $\delta^{34}S_{CAS}$ values

393     of the upper Muhu Formation. The lower but more variable $\delta^{34}S_{CAS}$ values with elevated Mg/Ca

394     from the higher energy peritidal environments is the inverse facies relationship observed in Present

395     et al., (2019). This suggests that dolomitization influences more local controls on $\delta^{34}S_{CAS}$ evolution

396     in this basin and highlights the importance of assessing which facies best preserve $\delta^{34}S_{CAS}$ in a

397     given carbonate succession. Overall this information suggests that late-stage post-depositional

398     fluids (meteoric or burial) did not reset the isotope proxies throughout the Paatsalu core, and that

399     variability in the isotopic compositions must result from smaller scale, more localized processes.

400

*5.1.2 Sulfide oxidation: decreased $\delta^{34}S_{CAS}$ and $\delta^{18}O_{CAS}$*

Early marine diagenetic processes can generate correlated local increases and decreases in $\delta^{34}S_{SO4}$ and $\delta^{18}O_{SO4}$ of porewater, which can then be retained in the (re)precipitating carbonate $\delta^{34}S_{CAS}$ and $\delta^{18}O_{CAS}$ values (e.g. Goldberg et al., 2005; Rennie and Turchyn, 2014). Sulfide (and pyrite) is $^{34}S$-depleted relative to sulfate due to MSR, and when it is oxidized the product sulfate will inherit these lower $\delta^{34}S$ values. The same sulfide that is oxidized will incorporate oxygen from the ambient fluid which lowers the resultant $\delta^{18}O_{SO4}$ (Goldberg et al., 2005; Newton et al., 2004). Negative correlations in plots of $\delta^{34}S_{CAS}$ vs. CAS and/or pyrite abundance can indicate the influence of pyrite oxidation, particularly during laboratory extractions (Marenco et al., 2008a). In the Paatsalu data, there are no general correlations between $\delta^{34}S_{CAS}$ and CAS or pyrite abundance (Fig. 5B and C) meaning that influence of pyrite oxidation during laboratory extraction on sulfur, and therefore oxygen isotopes, in CAS can be excluded. However, samples with the lowest $\delta^{34}S_{CAS}$ values (< 15‰; much lower than what is observed during laboratory extraction, Marenco et al., 2008a) also contain the greatest, yet also most variable, abundance of CAS (Fig. 5B). This correlation is not systematic but most likely reflects variable sulfide/pyrite oxidation and subsequent incorporation of sulfate as CAS under oxic conditions, a process known to impact modern sediments (Percak-Dennett et al., 2017). The correlation of anomalously low $\delta^{34}S_{CAS}$ values (3-15‰), compared to Ordovician-Silurian seawater from evaporite minerals (25.5‰; Kampschulte and Strauss, 2004), with similarly low $\delta^{18}O_{CAS}$ values (-1.7-10‰; Fig. 6A) is further evidence to support that these samples have been the most influenced by sulfide oxidation (e.g. Goldberg et al., 2005). Samples with $\delta^{34}S_{CAS}$ values 20-25‰ may also have incorporated sulfur isotope values from locally oxidized sulfide, although to a lesser extent.

423        Depositional environmental conditions give rise to localized decreases in $\delta^{34}$S and $\delta^{18}$O of

424    ambient seawater (porewater) sulfate. In shallow water environments, the frequency of

425    sedimentary reworking increases (e.g. by bioturbation, tides and storms), resulting in punctuated

426    oxidation of the pore fluid as well as frequent exposure to air. This is likely to have influenced

427    samples with moderately low $\delta^{34}$S$_{CAS}$ (20-25‰) which are predominantly observed within

428    wackestone and packstone facies (Fig. 5D). Additionally, tidal environments are influenced by

429    continental freshwater, where weathering of pyrite on land causes low $\delta^{34}$S values of riverine

430    sulfate. However, freshwater typically has lower concentrations of sulfate compared to seawater

431    and would result in a decrease of CAS abundance (Gill et al., 2008). Although continental-derived

432    fluids may interact with carbonates at any time, we suspect that the influence of continental fluids

433    is minor and may only be preserved in a small number of samples from the Muhu Formation (Fig.

434    2 at 4.5 and 22.7 m) with those samples containing low CAS abundance, low Sr, and high Fe and

435    Mn. Although these geochemical parameters are consistent with possible meteoric influence,

436    $\delta^{18}$O$_{Carb}$ values do not support a clear meteoric influence on these samples. Thus an alternate

437    explanation for very low $\delta^{34}$S$_{CAS}$ values (down to 3‰) is required, such as dolomitization coupled

438    with sulfide oxidation as discussed above.

439

440    *5.1.3 Microbial Sulfate Reduction: increased $\delta^{34}$S$_{CAS}$ and $\delta^{18}$O$_{CAS}$*

441    Microbial sulfate reduction, considered an early marine diagenetic process, results in correlated

442    increases in sulfur and oxygen isotopic compositions in residual porewater sulfate, particularly

443    under closed system conditions where the rate of sulfate consumption in porewater is greater than

444    the rate sulfate is replenished by the diffusion of seawater (Goldberg et al., 2005). MSR increases

445    alkalinity, promoting carbonate precipitation in pore spaces (Baumgartner et al., 2006; Berner et

446 al., 1970). Thus, newly precipitating and/or recrystallizing carbonate has the potential to

447 incorporate these evolved porewater sulfate signals into CAS, elevating $\delta^{34}S_{CAS}$ and $\delta^{18}O_{CAS}$

448 values (Antler et al., 2013; Goldberg et al., 2005; Rennie and Turchyn, 2014).

449 In addition to porewater sulfate isotopes evolving with increasing depth beneath the sediment

450 surface, platform-scale progressive evolution of pore fluids can also occur, associated with

451 basinward migration of platform-top brines (Al-Helal et al., 2012) or shoreward migration of

452 seawater (e.g. Jones et al., 2019). These processes would also result in progressively increasing

453 porewater $\delta^{34}S_{SO4}$ and $\delta^{18}O_{SO4}$ along the direction of the flow path (vertical and lateral), as

454 continued MSR will progressively remove $^{32}S$. Evidence for platform-scale evolution of pore-

455 fluids is observed in the stratal geometry of the dolomite between the Paatsalu and Viki cores; all

456 samples from the Jaani and Muhu Formations show partial dolomitization in the Paatsalu core, yet

457 only samples from the upper Jaani and lower Jaagarahu Formation (time correlative to the Muhu

458 Formation) in the Viki core are partially dolomitized (Richardson et al., 2019a). In this case, the

459 chemical evolution of local pore-fluids during basinward migration from the shallow-water facies

460 (e.g. upper Jaani Formation, Viki core), would result in increased $\delta^{34}S_{SO4}$ in deeper water facies

461 (e.g. Jaani Formation, Paatsalu core). We speculate that the evolution of $\delta^{34}S_{SO4}$ and $\delta^{18}O_{SO4}$ in

462 pore spaces in shallow-water environments (due to MSR), and the migration of these fluids to

463 deeper environments might best explain the increase in $\delta^{34}S_{CAS}$ values (~30‰) in the middle of

464 the deep-water facies of the Jaani Formation in the Paatsalu core. This hypothesized migration of

465 pore fluids associated with dolomitizing fluids may be recorded in other isotope systems such as

466 $\delta^{44}Ca$ and $\delta^{26}Mg$, where paired $\delta^{44}Ca$ and $\delta^{26}Mg$ data could differentiate between fluid- and

467 sediment-buffered conditions during dolomitization. An examination of cross-plots of $\delta^{18}O_{CAS}$ vs.

468 $\delta^{34}S_{CAS}$ can help assess closed-system behavior associated with parallel positive shifts in oxygen

469 and sulfur isotopic compositions (Fig. 6). Values of $\delta^{34}S_{CAS}$ and $\delta^{18}O_{CAS}$ are positively correlated

470 (Fig. 6A), even when removing the subset of samples most influenced by sulfide oxidation (Fig.

471 6B). Similar correlations of $\delta^{34}S_{CAS}$ and $\delta^{18}O_{CAS}$ relationships are observed in the Viki core (Fig.

472 7A and 7B). Wackestone, packstone, and partially dolomitic marlstone facies show the strongest

473 $\delta^{34}S_{CAS}$-$\delta^{18}O_{CAS}$ correlation (Fig. 6C). Additionally, $\delta^{34}S_{CAS}$ shows greater variability in

474 wackestone and packstone facies compared to the dolomitic marlstone (Fig. 5D and 6C),

475 potentially attributable to the increased, yet pulsed, nature of shallow-water sedimentation (e.g.

476 Aller et al., 2004; Aller et al., 2010; Richardson et al., 2019a).

477 In the absence of any correlations between late-stage diagenetic indicators (e.g. $\delta^{13}C_{carb}$ vs.

478 $\delta^{18}O_{carb}$, see *5.1.1*), Mn/Sr can be used as an indication of precipitation or recrystallization in

479 anoxic pore fluid during early marine diagenesis (e.g. Turchyn et al., 2009b). This tool is based on

480 low Mn/Sr ratios in modern seawater (i.e. $< 4x10^{-7}$, see Chester, 1990) and high Mn/Sr in evolved

481 waters (Brand and Veizer, 1980), suggesting that anoxic pore fluids that evolved from seawater

482 will concentrate Mn. As such, Mn/Sr ratios are used as a screening tool, typically assigning a

483 threshold above which samples are excluded from primary geochemical interpretation of $^{87}Sr/^{86}Sr$,

484 $\delta^{13}C$ and $\delta^{34}S_{SO4}$ (Bartley et al., 2001; Fölling and Frimmel, 2002; Gómez Peral et al., 2007;

485 Tostevin et al., 2017; Turchyn et al., 2009). However, Mn/Sr values < 1 have been found in modern

486 carbonates substantially affected by early marine diagenesis (Higgins et al., 2018), calling into

487 question the usefulness of a Mn/Sr threshold in ancient carbonates that have likely experienced

488 more diagenesis than modern carbonate platforms. We use Mn/Sr as an additional assessment of

489 $\delta^{34}S_{CAS}$ values that have been most impacted by MSR (i.e. carbonate precipitating or

490 recrystallizing in anoxic conditions associated with sulfate reduction). In this context, a majority

491 of Paatsalu samples have a recrystallized signature (Fig. 6D). However, these samples fall into two

492    groups, samples with Mn/Sr < 3.5 from the shallow-water facies in the Nurmekund and Rumba

493    Formations, and samples Mn/Sr > 3.5 from the base of the Velise to the top of the core. Based on

494    the grouping of samples, $\delta^{34}S_{CAS}$ vs. $\delta^{18}O_{CAS}$ is replotted in these groups and a positive correlation

495    between these proxies is only observed for samples with Mn/Sr > 3.5 (Fig. 6E). Similar

496    correlations are present in the Viki samples, yet with a slightly lower Mn/Sr grouping of 3. In the

497    Viki core, a majority of samples with Mn/Sr > 3 are from the Muhu and Jaani Formations, with a

498    lesser contribution from the Velise Formation (Fig. 7C and 7D). A majority of the samples with

499    Mn/Sr > 3.5 also have higher Mg/Ca ratios and are partially dolomitized, yet this is not always the

500    case, even for the Viki core. These observations suggest that the enrichment in $\delta^{34}S_{CAS}$ and $\delta^{18}O_{CAS}$

501    tracks newly precipitating carbonate or recrystallization in a marine diagenetic realm under

502    isotopically evolving anoxic pore fluids.

503           We infer that correlated increases in $\delta^{34}S_{CAS}$ and $\delta^{18}O_{CAS}$ in Paatsalu strata record evolving

504    porewater sulfate associated with varying amounts of MSR and varying rates of carbonate

505    recrystallization in the different paleoenvironments. In this framework, the most evolved

506    porewater sulfate values plot in the upper-right and the least evolved (and therefore most

507    representative of seawater $\delta^{34}S_{SO4}$ and $\delta^{18}O_{SO4}$) samples are in the bottom-left quadrant in $\delta^{34}S_{CAS}$

508    vs. $\delta^{18}O_{CAS}$ (Fig. 6B; excluding samples clearly affected by sulfide oxidation). We suggest that

509    seawater $\delta^{34}S_{SO4}$ was approximately 27-28‰ and $\delta^{18}O_{SO4}$ was 14-15‰ during deposition of

510    Paatsalu strata based on visual clustering of samples (Fig 6C) and the frequency of samples with

511    these values in the dolomitized marlstone (i.e. deep-water facies). This deep-water facies likely

512    formed in more open connectivity with seawater with respect to the shallow-water settings. This

513    $\delta^{34}S_{SO4}$ range agrees with time-equivalent $\delta^{34}S_{CAS}$ values from brachiopods from Gotland (Present,

514    2018) although is somewhat heavier than time-equivalent evaporite data (Kampschulte and

515   Strauss, 2004). Progressive MSR and sulfide oxidation can increase and decrease porewater

516   $\delta^{34}S_{SO4}$ and $\delta^{18}O_{SO4}$, respectively, relative to coeval seawater (Goldberg et al., 2005). We observe

517   here that these signals can be preserved in recrystallized carbonates as CAS. This observation can,

518   in part, explain the elevated variability in many deep-time $\delta^{34}S_{CAS}$ records that cannot otherwise

519   be reconciled with behavior of the relatively invariant marine sulfate reservoir.

520

521   *5.1.4 Relative timing of carbonate diagenesis*

522   As discussed, many factors can contribute to the measured isotope signal in carbonate sediments.

523   Disentangling these processes can help to identify the *most primary* values in a given section. We

524   suggest the following diagenetic sequence of early marine and late marine diagenesis, followed by

525   dolomitization, for the evolution of sulfur isotope proxies in the Paatsalu core. First, early marine

526   diagenetic MSR increases pore fluid $\delta^{34}S$ values where carbonate cement and pyrite form. In

527   shallow-water environments, bioturbation, tidal activity, and wave action disturb the isotope

528   stratification in the sediment (e.g. Aller, 2004; Aller et al., 2010) by introducing seawater sulfate

529   into the sediment, and by potentially oxidizing pore water sulfide. Ultimately, this generates

530   isotopic variability between precipitating components. Proximity to the paleoshoreline (e.g.

531   interbedded arenite, Muhu Formation, Paatsalu core) influences the frequency of tidal reworking,

532   aerial exposure and interaction with continental water, which can result in localized sulfide

533   oxidation and subsequent incorporation of non-marine $\delta^{34}S_{CAS}$ values during carbonate formation

534   or recrystallization. These processes are dependent on depositional environment conditions and

535   can be considered syndepositional. Second, post-depositional marine diagenesis is common to

536   carbonate platforms, resulting in carbonate recrystallization (Christ et al., 2015). In this case,

537   platform-scale evolution of pore fluids from shallow-water environments (with distilled isotope

538    ratios) in the eastern portion of the basin migrated to deeper environments resulting in an increase

539    of $\delta^{34}S_{CAS}$ of precipitating/recrystallizing carbonate in distal settings. Dolomitizing fluids in the

540    Baltoscandian basin were associated with different styles of diagenesis and occurred

541    synchronously and/or post-dated late marine diagenetic processes. In the nearshore environments,

542    these dolomitizing fluids, with sulfate sourced in part by sulfide oxidation, may have had a greater

543    impact, decreasing $\delta^{34}S_{CAS}$ values in the newly formed dolomite (although this requires additional

544    detailed petrographic investigations to elucidate). Importantly the early marine 'syndepositional'

545    processes are inherent to most carbonate platforms throughout Earth history. Additional insight

546    into the sequence of diagenetic processes could be gained in the future through component-specific

547    (i.e. individual fossil, cement or micrite phases) isotope analyses, such as via MC-ICP-MS

548    (Johnson et al., 2020; Present et al., 2019, 2015) or SIMS (Bryant et al., 2020; Xiao et al., 2020).

549

550    *5.2 Intra-basin isotope variability*

551    *5.2.1 Carbon isotopes*

552    The existence of multiple time-equivalent chemostratigraphic profiles provides a means to assess

553    the reproducibility of data across the Baltoscandian Basin. Compared to the Viki core, the

554    chemostratigraphic record of the Paatsalu core is more complete in the lower mid-Llandovery, but

555    is condensed in the upper Llandovery to the early-Wenlock due to differences in sedimentation

556    rate and erosion (Rubel et al., 2007). The overall trends in paired $\delta^{13}C_{carb}$-$\delta^{13}C_{org}$ are consistent

557    between the two drill cores (Fig. 3) except for a slight decrease in $\delta^{13}C_{org}$ during the peak of the

558    $\delta^{13}C_{carb}$ isotope excursion associated with the IBE in the Paatsalu data. This anti-correlation in

559    carbon isotopes in the Jaani Formation is site-specific (Richardson et al., 2019a; Rose et al., 2019;

560    Young et al., 2019), reflecting an increase in the apparent biological fractionation. The magnitude

561    of the $\delta^{13}C_{carb}$ isotope excursion during the IBE is ~ 0.2‰ lower in Paatsalu compared to the Viki

562 core and they are both ~ 0.5-0.8‰ lower than the record from Gotland (Rose et al., 2019). Such

563 differences in the magnitude of carbon isotope variation between Estonia and Gotland could be

564 due to variations in the local $\delta^{13}C_{DIC}$ gradient generated by the biological pump, exporting more

565 $^{13}$C-depleted carbon to deeper settings specifically at the Gotland site during the IBE, which

566 resulted in a greater increase in $\delta^{13}C_{carb}$ of the shallow water carbonates being deposited at Gotland.

567 Data across the IBE on Gotland have shown that systematic variations in $\delta^{13}C_{org}$ of different

568 organism groups may be a few per mil (Vandenbroucke et al., 2013). Thus, the extinction event

569 and associated paleoecological turnovers could have influence on average isotopic values.

570 Additionally, gradients across a carbonate platform can generate $\delta^{13}C_{carb}$ variability of up to 5‰

571 due to enhanced accumulation of $^{13}$C-enriched aragonite sediment on the platform compared to

572 $^{13}$C-depleted pelagic material (Geyman et al., 2021; Swart and Eberli, 2005), as well as fluid- vs.

573 sediment-buffered lithification and early marine diagenesis (Higgins et al., 2018; Jones et al.,

574 2019). Either of these processes could be the cause of the 0.2‰ difference in $\delta^{13}C_{carb}$ between the

575 Paatsalu and Viki core within the Jaani Formation.

576 Early Silurian carbon isotope records from the Baltoscandian basin record similar

577 stratigraphic signals, possibly representing a global perturbation of the carbon cycle, as evidenced

578 by the number of sections worldwide that retain coeval carbon isotopic excursions coincident with

579 the IBE (e.g. Azmy et al., 1998; Calner, 2008; Cramer and Saltzman, 2005; Lehnert et al., 2010;

580 Rose et al., 2019; Young et al., 2019). The duration of the carbon isotope excursion expressed

581 globally is < 2 Myr (Cramer et al., 2010; Nestor, 2010), which is sufficiently long for the global

582 carbon cycle to respond to a perturbation (Kump and Arthur, 1999). Previous research suggests

583 that a perturbation to the DIC reservoir (through a decrease in organic carbon burial) enhanced by

584 glacioeustatic sea level change may be the cause of the carbon isotope excursion coincident with

585  the IBE (Cramer and Saltzman, 2005; Lehnert et al., 2010; Munnecke et al., 2010; Richardson et

586  al., 2019). Local depositional effects on $\delta^{13}C$ between the sites examined are likely superimposed

587  on any global carbon isotope signal. It is important to note, however, that the effect of mineralogy

588  and fluid- versus sediment-buffered early marine diagenesis across a platform cannot be

589  discounted as a mechanism for the observed carbon isotope excursion in the Baltoscandian Basin,

590  especially given that the IBE is commonly associated with a eustatic sea level induced facies

591  change (Rose et al. 2019). Further data (e.g., $\delta^{44}Ca$ and $\delta^{26}Mg$) are required to determine if the

592  IBE $\delta^{13}C$ signal truly reflects a perturbation to the global carbon cycle or is the result of local and

593  facies-specific processes (Higgins et al., 2018; Jones et al., 2019).

594

595  *5.2.2 Sulfur isotopes*

596  No coherent basin-wide sulfur isotope excursion is observed during the IBE. The sulfur isotope

597  records are distinct in magnitude, variability and stratigraphic expression between the Paatsalu and

598  Viki cores (Fig. 3; Richardson et al. 2019a) and, importantly, a paired $\delta^{34}S_{CAS}$-$\delta^{34}S_{pyr}$ excursion

599  during the IBE on Gotland (Rose et al., 2019) is not observed in either of the Estonian sections.

600  The absence of a coherent basin-wide $\delta^{34}S_{CAS}$-$\delta^{34}S_{pyr}$ excursion indicates the sulfur isotope records

601  of these sections are not proxies for the evolution of the global or even basinal sulfate reservoir.

602  This is further evidenced by comparing Wenlock $\delta^{34}S_{CAS}$-$\delta^{34}S_{pyr}$ with sections in the USA; paired

603  $\delta^{34}S_{CAS}$-$\delta^{34}S_{pyr}$ increases throughout the early Wenlock in Nevada, yet $\delta^{34}S_{CAS}$ decreases

604  throughout the early Wenlock in Tennessee (Young et al., 2019). The sulfur isotope values

605  between Paatsalu and Viki cores and outcrop in Gotland appear to be controlled by (local)

606  depositional and early marine diagenetic processes. Although local controls on $\delta^{34}S_{pyr}$ are

607  generally well-established (Aller et al., 2010; Bryant et al., 2019; Claypool, 2004; Liu et al., 2019;

608    Pasquier et al., 2017), the effect of site-specific depositional environment and early marine

609    diagenesis on $\delta^{34}S_{CAS}$ values is less well constrained (Fike et al., 2015; Present et al., 2019; Rennie

610    and Turchyn, 2014; Richardson et al., 2019a; Rose et al., 2019), and clearly merits further study.

611          While the changes in $\delta^{34}S_{CAS}$ and $\delta^{34}S_{pyr}$ between the Estonian cores are generally not

612    coeval in timing and/or magnitude, approximately similar trends between facies packages are

613    observed between the two drill cores, albeit at slightly different times in different places on the

614    carbonate platform. The $\delta^{34}S_{CAS}$ and $\delta^{34}S_{pyr}$ values are commonly more variable in shallow-water

615    carbonate facies, likely owing to higher sedimentation rate, increased labile organic carbon

616    delivery, increased reactive iron availability, and the episodic nature of reworking events. These

617    parameters result in the development of a closed-system pore water environment and distillation

618    of isotopes during MSR, that is then variably reset by tidal/storm reworking to a more open system

619    (Aller et al., 2010; Fike et al., 2015; Richardson et al., 2019a). This process of developing more

620    closed-system conditions, punctuated by reworking events that generate more open-system

621    conditions, is a continuous cycle and results in the isotopic variability of shallow-water carbonate

622    $\delta^{34}S_{CAS}$ and $\delta^{34}S_{pyr}$. Decreased variability in $\delta^{34}S_{CAS}$ and $\delta^{34}S_{pyr}$ occurs when there is lower

623    sedimentation rate, decreased labile organic carbon delivery, and/or decreased reactive iron

624    availability, in this case occurring under higher relative sea level, e.g. in the mid-Jaani Formation,

625    the deepest setting recorded in the core (Table 1; although this trend is also seen in $\delta^{34}S_{pyr}$ of the

626    shallow-water Rumba Formation). Different depositional environments form carbonates

627    composed of varying abundances of distinct components (cement, micrite, fossils and grains). The

628    components may form above or below the sediment water interface, during early marine diagenesis

629    or any time during fluid movement, resulting in variable CAS abundance and $\delta^{34}S_{CAS}$ (Present et

630    al., 2015; Richardson et al., 2019b). For example, carbonate components precipitating in the region

631    of MSR (where concentrations of dissolved sulfate are lower) may have an overall lower CAS

632    abundance (e.g. Richardson et al., 2019b). In a plot of 1/[CAS] vs $\delta^{34}S_{CAS}$, mixing of components

633    will fall on a straight line (Fig. 5B) (Present et al., 2015). Although systematic mixing is not clear,

634    the wackestone and packstone facies (typically having the widest variety of components) indicate

635    physical mixing of CAS abundance and $\delta^{34}S_{CAS}$ of different components from a single sample.

636    This is consistent with our interpretation that shallow-water carbonates (e.g. reef facies) can be

637    unreliable proxies for global seawater $\delta^{34}S_{CAS}$ (Richardson et al., 2019a).

638        The location on the carbonate platform and facies dependence is recorded as differences in

639    the $\delta^{34}S_{CAS}$ and $\delta^{34}S_{pyr}$ values of time-correlative formations between Paatsalu and Viki sites. This

640    site-specific depositional control is attributable to the relative effect of sea-level change at each

641    location (and therefore water energy), whereby proximity to the shoreline variably drives tidal,

642    biological and sedimentation processes. For example, during sea level low-stand in the mid-

643    Llandovery, shallow-water carbonate facies (marginal marine to outer shelf) were deposited at

644    both the Paatsalu and Viki sites. However, the Paatsalu site was closer to the shoreline and the

645    shallow-water facies recorded are vertical stacks of peritidal-lagoonal sequences to inner-mid shelf

646    facies in the Nurmekund and Rumba formations, respectively. In contrast, those formations in the

647    Viki core consist of backreef to proximal shelf facies (Richardson et al., 2019a). The lower $\delta^{34}S_{CAS}$

648    values and higher sample-to-sample variability in these two formations from Paatsalu compared

649    to the Viki core reflect increased frequency of sediment reworking from wave-action and tidal

650    processes in peritidal environments. The result is a fluid-buffered system where the $\delta^{34}S$ of the

651    precipitating CAS is moderated by pore fluid $\delta^{34}S_{SO4}$ that is frequently replenished by seawater

652    (Present et al., 2019). The average $\delta^{34}S_{CAS}$ of the Nurmekund and Rumba formations in the

653    Paatsalu core is 28.9 and 24.8‰ respectively, compared to 34.38‰ and 17.3 ‰ (skewed by 4

654 samples) in the Viki core. These shallow-water facies in the Paastsalu core are closer to previous

655 estimates for $\delta^{34}S_{SO4}$ Silurian seawater (Kampschulte and Strauss, 2004; Present, 2018).

656

657 *5.2.3 Oxygen isotopes*

658 Oxygen isotopes of sulfate substantiate our conclusion that sulfur isotope signatures in the

659 Baltoscandian Basin preserve a local, early marine diagenetic signature. $\delta^{18}O_{CAS}$ values between

660 the Paatsalu and Viki cores are similar (~ 10-20‰; Fig. 3); however, there is greater variability in

661 the Paatsalu drill core. Lithology-specific $\delta^{34}S_{CAS}$-$\delta^{18}O_{CAS}$ data show similar, positive correlations

662 between facies packages in the Paatsalu and Viki drill cores (Fig. 7B and C). Mn/Sr ratios (Fig.

663 7C and D) and previous analyses support the idea that bulk isotope proxies from the Viki core have

664 not been reset by non-marine diagenesis (Richardson et al., 2019a). We suggest that the observed

665 paired $\delta^{34}S_{CAS}$-$\delta^{18}O_{CAS}$ enrichments are recording an evolving diagenetic porewater signature at

666 these locations, yet is also observed in a handful of samples from deep-water carbonate facies

667 indicative of platform-scale migration of fluids and/or carbonate recrystallization at depth within

668 the anoxic zone of the sediment.

669 The frequency and visible clustering of $\delta^{18}O_{CAS}$ values from marlstone facies (i.e. deep-

670 water facies in open connectivity with seawater) is the best assessment for most primary $\delta^{18}O_{CAS}$

671 and are comparable between the cores (14–15‰ in Paatsalu and 14-17‰ in Viki). These $\delta^{18}O_{CAS}$

672 values are similar to $\delta^{18}O_{SO4}$ of age-equivalent evaporites (Claypool et al., 1980). All other $\delta^{18}O_{CAS}$

673 values in the sections reported here, i.e. increased or decreased relative to 14-15‰, are not

674 recording changes to the global sulfur cycle. Instead, $\delta^{18}O_{CAS}$ variably records an early marine

675 diagenetic signal as a function of depositional setting, responding similarly to patterns observed in

676      $\delta^{34}S_{CAS}$. More sections should be sampled for paired $\delta^{34}S_{CAS}$-$\delta^{18}O_{CAS}$ analyses to identify the least

677      evolved values that best approximate seawater $\delta^{34}S$-$\delta^{18}O$.

678

679      **6.0 Conclusions**

680      Paired $\delta^{13}C_{carb}$-$\delta^{13}C_{org}$ data from deep-water carbonates in the Paatsalu core from the Eastern

681      portion of the Baltoscandian Basin record a positive carbon isotope excursion coincident with the

682      Ireviken Bioevent (IBE), but of slightly lower magnitude to that preserved in the equivalent

683      shallow-water formations in the western portion of the Baltoscandian basin. Variability in carbon

684      isotope composition is an expression of local depositional settings modifying a likely global

685      perturbation. In contrast, there is no basin-wide sulfur isotopic excursion observed during the IBE;

686      in the slightly more proximal setting in the east compared to the same facies packages in the west

687      basin, sulfur and oxygen isotopes record distinct stratigraphic signals, a consequence of differing

688      early marine diagenetic processes in shallow- versus deep-water settings. Paired $\delta^{34}S_{CAS}$-$\delta^{34}S_{pyr}$

689      are variable in the former and more uniform in the latter, similar to observations from paired

690      $\delta^{34}S_{CAS}$-$\delta^{34}S_{pyr}$ in the previously studied Viki core. Paired $\delta^{34}S_{CAS}$-$\delta^{18}O_{CAS}$ data preserve signatures

691      of diagenetic isotopic distillation as a result of progressive MSR in porewaters. Further, proximity

692      to paleoshorelines may also affect shallow-water $\delta^{34}S_{CAS}$, $\delta^{34}S_{pyr}$ and $\delta^{18}O_{CAS}$ values due to tidal

693      and potentially storm disruption of sediment stratification and isotope distillation. Later marine

694      diagenesis and dolomitization resulted in basinward platform-scale progressive evolution of pore

695      fluids, such that deep-water facies experienced increases in $\delta^{34}S_{CAS}$ and $\delta^{18}O_{CAS}$ values, while

696      shallow-water environments have signals associated with sulfide oxidation incorporated during

697      dolomitization. The best preserved values for $\delta^{34}S_{CAS}$ and $\delta^{18}O_{CAS}$ are near 27-28‰ and 14-15‰,

698      respectively, based on clustering and frequency of values in $\delta^{34}S_{CAS}$ vs $\delta^{18}O_{CAS}$ from marlstone

699     units. These values are in broad agreement with temporal time-equivalent evaporite records. Future

700     studies aiming to interpret $\delta^{34}S_{CAS}$-$\delta^{34}S_{pyr}$ data in terms of sulfur cycling should include

701     depositional context and paired $\delta^{34}S_{CAS}$-$\delta^{18}O_{CAS}$ to assess the impact of isotope distillation.

702

712

713     **References**

714     Adams, D.D., Hurtgen, M.T., Sageman, B.B., 2010. Volcanic triggering of a biogeochemical

715         cascade during Oceanic Anoxic Event 2. Nat. Geosci. 3, 201–204.

716         https://doi.org/10.1038/ngeo743

717     Ahm, A.S.C., Bjerrum, C.J., Blättler, C.L., Swart, P.K., Higgins, J.A., 2018. Quantifying early

718         marine diagenesis in shallow-water carbonate sediments. Geochim. Cosmochim. Acta 236,

719         140–159. https://doi.org/10.1016/j.gca.2018.02.042

720     Al-Helal, A.B., Whitaker, F.F., Xiao, Y., 2012. Reactive transport modeling of brine reflux:

721         dolomitization, anhydrite precipitation, and porosity evolution. J. Sediment. Res. 82, 196–

722         215. https://doi.org/10.2110/jsr.2012.14

723     Aller, R.C., 2004. Conceptual models of early diagenetic processes: The muddy seafloor as an

724         unsteady, batch reactor. J. Mar. Res. 62, 815–835.

725         https://doi.org/10.1357/0022240042880837

726     Aller, R.C., Madrid, V., Chistoserdov, A., Aller, J.Y., Heilbrun, C., 2010. Unsteady diagenetic

727    processes and sulfur biogeochemistry in tropical deltaic muds: Implications for oceanic

728    isotope cycles and the sedimentary record. Geochim. Cosmochim. Acta 74, 4671–4692.

729    https://doi.org/10.1016/j.gca.2010.05.008

730  Antler, G., Turchyn, A. V., Rennie, V., Herut, B., Sivan, O., 2013. Coupled sulfur and oxygen

731    isotope insight into bacterial sulfate reduction in the natural environment. Geochim.

732    Cosmochim. Acta 118, 98–117. https://doi.org/10.1016/J.GCA.2013.05.005

733  Azmy, K., Veizer, J., Bassett, M.G., Copper, P., 1998. Oxygen and carbon isotopic composition

734    of Silurian brachiopods: Implications for coeval seawater and glaciations. Geol. Soc. Am.

735    Bull. 110, 1499. https://doi.org/10.1130/0016-7606(1998)110<1499:OACICO>2.3.CO;2

736  Baarli, B.G., Johnson, M.E., Antoshkina, A.I., 2003. Silurian Stratigraphy and Paleogeography

737    of Baltica, in: Silurian Lands and Seas. Paleogeography Outside of Laurentia. New York

738    State Museum, New York. New York State Museum Bulletin 493, 3-34.

739  Baldermann, A., Deditius, A.P., Dietzel, M., Fichtner, V., Fischer, C., Hippler, D., Leis, A.,

740    Baldermann, C., Mavromatis, V., Stickler, C.P., Strauss, H., 2015. The role of bacterial

741    sulfate reduction during dolomite precipitation: Implications from Upper Jurassic platform

742    carbonates. Chem. Geol. 412, 1–14. https://doi.org/10.1016/j.chemgeo.2015.07.020

743  Banner, J.L., Hanson, G.N., 1990. Calculation of simultaneous isotopic and trace element

744    variations during water-rock interaction with applications to carbonate diagenesis.

745    Geochim. Cosmochim. Acta 54, 3123–3137. https://doi.org/10.1016/0016-7037(90)90128-8

746  Bartley, J.K., Kah, L.C., 2004. Marine carbon reservoir, Corg-Ccarb coupling, and the evolution

747    of the Proterozoic carbon cycle. Geology 32, 129. https://doi.org/10.1130/G19939.1

748  Bartley, J.K., Semikhatov, M.A., Kaufman, A.J., Knoll, A.H., Pope, M.C., Jacobsen, S.B., 2001.

749    Global events across the Mesoproterozoic-Neoproterozoic boundary: C and Sr isotopic

750     evidence from Siberia. Precambrian Res. 111, 165–202. https://doi.org/10.1016/S0301-

751     9268(01)00160-7

752    Baumgartner, L.K., Reid, R.P., Dupraz, C., Decho, A.W., Buckley, D.H., Spear, J.R., Przekop,

753     K.M., Visscher, P.T., 2006. Sulfate reducing bacteria in microbial mats: Changing

754     paradigms, new discoveries. Sediment. Geol. 185, 131–145.

755     https://doi.org/10.1016/J.SEDGEO.2005.12.008

756    Berner, R.A., Scott, M.R., Thomlinson, C., 1970. Carbonate alkalinity in the pore waters of

757     anoxic marine sediments. Limnol. Oceanogr. 15, 544–549.

758     https://doi.org/10.4319/lo.1970.15.4.0544

759    Bottrell, S.H., Newton, R.J., 2006. Reconstruction of changes in global sulfur cycling from

760     marine sulfate isotopes. Earth-Science Rev. 75, 59–83.

761     https://doi.org/10.1016/J.EARSCIREV.2005.10.004

762    Brand, U., Veizer, J., 1980. Chemical Diagenesis of a Multicomponent Carbonate System--1:

763     Trace Elements. SEPM J. Sediment. Res. Vol. 50, 1219–1236.

764     https://doi.org/10.1306/212F7BB7-2B24-11D7-8648000102C1865D

765    Brett, C.E., Boucot, A.J., Jones, B., 1993. Absolute depths of Silurian benthic assemblages.

766     Lethaia 26, 25–40. https://doi.org/10.1111/j.1502-3931.1993.tb01507.x

767    Bryant, R.N., Jones, C., Raven, M.R., Gomes, M.L., Berelson, W.M., Bradley, A.S., Fike, D.A.,

768     2019. Sulfur isotope analysis of microcrystalline iron sulfides using secondary ion mass

769     spectrometry imaging: Extracting local paleo-environmental information from modern and

770     ancient sediments. Rapid Commun. Mass Spectrom. 33, 491–502.

771     https://doi.org/10.1002/rcm.8375

772    Bryant, R.N., Jones, C., Raven, M.R., Owens, J.D., Fike, D.A., 2020. Shifting modes of iron

773      sulfidization at the onset of OAE-2 drive regional shifts in pyrite δ34S records. Chem. Geol.

774      553, 119808. https://doi.org/10.1016/j.chemgeo.2020.119808

775  Burdett, J.W., Arthur, M.A., Richardson, M., 1989. A Neogene seawater sulfur isotope age curve

776      from calcareous pelagic microfossils. Earth Planet. Sci. Lett. 94, 189–198.

777      https://doi.org/10.1016/0012-821X(89)90138-6

778  Calner, M., 2008. Silurian global events – at the tipping point of climate change, in: Mass

779      Extinction. Springer Berlin Heidelberg, Berlin, Heidelberg, pp. 21–57.

780      https://doi.org/10.1007/978-3-540-75916-4_4

781  Canfield, D.E., 2001. Biogeochemistry of sulfur isotopes. Stable Isot. Geochemistry 43, 607–

782      636. https://doi.org/10.1515/9781501508745-015

783  Canfield, D.E., Raiswell, R., Westrich, J.T., Reaves, C.M., Berner, R.A., 1986. The use of

784      chromium reduction in the analysis of reduced inorganic sulfur in sediments and shales.

785      Chem. Geol. 54, 149–155. https://doi.org/10.1016/0009-2541(86)90078-1

786  Chester, R., 1990. Trace elements in the oceans, in: Marine Geochemistry. Springer Netherlands,

787      pp. 346–421. https://doi.org/10.1007/978-94-010-9488-7_11

788  Chiba, H., Sakai, H., 1985. Oxygen isotope exchange rate between dissolved sulfate and water at

789      hydrothermal temperatures. Geochim. Cosmochim. Acta 49, 993–1000.

790      https://doi.org/10.1016/0016-7037(85)90314-X

791  Christ, N., Immenhauser, A., Wood, R.A., Darwich, K., Niedermayr, A., 2015. Petrography and

792      environmental controls on the formation of Phanerozoic marine carbonate hardgrounds.

793      Earth-Science Rev. 151, 176–226. https://doi.org/10.1016/J.EARSCIREV.2015.10.002

794  Claypool, G.E., 2004. Ventilation of marine sediments indicated by depth profiles of pore water

795      sulfate and δ34S. Geochemical Soc. Spec. Publ. 9, 59–65. https://doi.org/10.1016/S1873-

796    9881(04)80007-5

797    Cocks, L.R.M., Torsvik, T.H., 2005. Baltica from the late Precambrian to mid-Palaeozoic times:

798        The gain and loss of a terrane's identity. Earth-Science Rev. 72, 39–66.

799        https://doi.org/10.1016/J.EARSCIREV.2005.04.001

800    Cramer, B.D., Brett, C.E., Melchin, M.J., Männik, P., Kleffner, M.A., Mclaughlin, P.I., Loydell,

801        D.K., Munnecke, A., Jeppsson, L., Corradini, C., Brunton, F.R., Saltzman, M.R., 2011.

802        Revised correlation of Silurian Provincial Series of North America with global and regional

803        chronostratigraphic units and $\delta 13$Ccarb chemostratigraphy. Lethaia 44, 185–202.

804        https://doi.org/10.1111/j.1502-3931.2010.00234.x

805    Cramer, B.D., Loydell, D.K., Samtleben, C., Munnecke, A., Kaljo, D., Männik, P., Martma, T.,

806        Jeppsson, L., Kleffner, M.A., Barrick, J.E., Johnson, C.A., Emsbo, P., Joachimski, M.M.,

807        Bickert, T., Saltzman, M.R., 2010. Testing the limits of Paleozoic chronostratigraphic

808        correlation via high-resolution (<500 k.y.) integrated conodont, graptolite, and carbon

809        isotope ($\delta 13$Ccarb) biochemostratigraphy across the llandovery-Wenlock (Silurian)

810        boundary: Is a unified Phanerozoic. Bull. Geol. Soc. Am. 122, 1700–1716.

811        https://doi.org/10.1130/B26602.1

812    Cramer, B.D., Saltzman, M.R., 2005. Sequestration of 12C in the deep ocean during the early

813        Wenlock (Silurian) positive carbon isotope excursion. Palaeogeogr. Palaeoclimatol.

814        Palaeoecol. 219, 333–349. https://doi.org/10.1016/J.PALAEO.2005.01.009

815    Eldridge, D.L., Guo, W., Farquhar, J., 2016. Theoretical estimates of equilibrium sulfur isotope

816        effects in aqueous sulfur systems: Highlighting the role of isomers in the sulfite and

817        sulfoxylate systems. Geochim. Cosmochim. Acta 195, 171–200.

818        https://doi.org/10.1016/J.GCA.2016.09.021

819    Erhardt, A.M., Turchyn, A. V., Dickson, J.A.D., Sadekov, A.Y., Taylor, P.D., Wilson, M.A.,

820        Scott, P., Schrag, D.P., 2020. Chemical Composition of Carbonate Hardground Cements as

821        Reconstructive Tools for Phanerozoic Pore Fluids. Geochemistry, Geophys. Geosystems 21.

822        https://doi.org/10.1029/2019GC008448

823    Fichtner, V., Strauss, H., Immenhauser, A., Buhl, D., Neuser, R.D., Niedermayr, A., 2017.

824        Diagenesis of carbonate associated sulfate. Chem. Geol. 463, 61–75.

825        https://doi.org/10.1016/J.CHEMGEO.2017.05.008

826    Fike, D.A., Bradley, A.S., Rose, C. V., 2015. Rethinking the Ancient Sulfur Cycle. Annu. Rev.

827        Earth Planet. Sci. 43, 593–622. https://doi.org/10.1146/annurev-earth-060313-054802

828    Fölling, P.G., Frimmel, H.E., 2002. Chemostratigraphic correlation of carbonate successions in

829        the Gariep and Saldania Belts, Namibia and South Africa. Basin Res. 14, 69–88.

830        https://doi.org/10.1046/j.1365-2117.2002.00167.x

831    Garrels, R.M., Lerman, A., 1981. Phanerozoic cycles of sedimentary carbon and sulfur

832        (isotopes/sediment cycles/natural oxygen reservoirs). Geology 78, 4652–4656.

833    Geyman, E.C., Maloof, A.C., Dyer, B., 2021. How is sea level change encoded in carbonate

834        stratigraphy? Earth Planet. Sci. Lett. 560, 116790.

835        https://doi.org/10.1016/j.epsl.2021.116790

836    Gill, B.C., Lyons, T.W., Frank, T.D., 2008. Behavior of carbonate-associated sulfate during

837        meteoric diagenesis and implications for the sulfur isotope paleoproxy. Geochim.

838        Cosmochim. Acta 72, 4699–4711. https://doi.org/10.1016/J.GCA.2008.07.001

839    Gill, B.C., Lyons, T.W., Saltzman, M.R., 2007. Parallel, high-resolution carbon and sulfur

840        isotope records of the evolving Paleozoic marine sulfur reservoir. Palaeogeogr.

841        Palaeoclimatol. Palaeoecol. 256, 156–173. https://doi.org/10.1016/J.PALAEO.2007.02.030

842    Goldberg, T., Poulton, S.W., Strauss, H., 2005. Sulphur and oxygen isotope signatures of late

843        Neoproterozoic to early Cambrian sulphate, Yangtze Platform, China: Diagenetic

844        constraints and seawater evolution. Precambrian Res. 137, 223–241.

845        https://doi.org/10.1016/J.PRECAMRES.2005.03.003

846    Gómez Peral, L.E., Poiré, D.G., Strauss, H., Zimmermann, U., 2007. Chemostratigraphy and

847        diagenetic constraints on Neoproterozoic carbonate successions from the Sierras Bayas

848        Group, Tandilia System, Argentina. Chem. Geol. 237, 109–128.

849        https://doi.org/10.1016/j.chemgeo.2006.06.022

850    Halverson, G.P., Dudás, F.Ö., Maloof, A.C., Bowring, S.A., 2007. Evolution of the 87Sr/86Sr

851        composition of Neoproterozoic seawater. Palaeogeogr. Palaeoclimatol. Palaeoecol. 256,

852        103–129. https://doi.org/10.1016/J.PALAEO.2007.02.028

853    Higgins, J.A., Blättler, C.L., Lundstrom, E.A., Santiago-Ramos, D.P., Akhtar, A.A., Crüger

854        Ahm, A.-S., Bialik, O., Holmden, C., Bradbury, H., Murray, S.T., Swart, P.K., 2018.

855        Mineralogy, early marine diagenesis, and the chemistry of shallow-water carbonate

856        sediments. Geochim. Cosmochim. Acta 220, 512–534.

857        https://doi.org/10.1016/J.GCA.2017.09.046

858    Hints, O., Killing, M., Männik, P., Nestor, V., 2006. Frequency patterns of chitinozoans,

859        scolecodonts, and conodonts in the upper Llandovery and lower Wenlock of the Paatsalu

860        core, western Estonia. Proc. Est. Acad. Sci. Geol. 55, 128–155.

861    Husson, J.M., Higgins, J.A., Maloof, A.C., Schoene, B., 2015. Ca and Mg isotope constraints on

862        the origin of Earth's deepest δ13C excursion. Geochim. Cosmochim. Acta 160, 243–266.

863        https://doi.org/10.1016/J.GCA.2015.03.012

864    Jeppsson, L., 1997. The anatomy of the mid-Early Silurian Ireviken Event and a Scenario of P-S

865      Events, in: Paleontological Events: Stratigraphic, Ecological and Evolutionary Implications.

866      pp. 451–492.

867 Johnson, D.L., Grossman, E.L., Webb, S.M., Adkins, J.F., 2020. Brachiopod $\delta^{34}S_{CAS}$

868      microanalyses indicate a dynamic, climate-influenced Permo-Carboniferous sulfur cycle.

869      Earth Planet. Sci. Lett. 546, 116428. https://doi.org/10.1016/j.epsl.2020.116428

870 Jones, D.S., Brothers, R.W., Ahm, A.-S.C., Slater, N., Higgins, J.A., Fike, D.A., 2019. Sea level,

871      carbonate mineralogy, and early diagenesis controlled $\delta^{13}C$ records in Upper Ordovician

872      carbonates. Geology. https://doi.org/10.1130/g46861.1

873 Jones, D.S., Fike, D.A., 2013. Dynamic sulfur and carbon cycling through the end-Ordovician

874      extinction revealed by paired sulfate–pyrite $\delta^{34}S$. Earth Planet. Sci. Lett. 363, 144–155.

875      https://doi.org/10.1016/j.epsl.2012.12.015

876 Kah, L.C., Lyons, T.W., Frank, T.D., 2004. Low marine sulphate and protracted oxygenation of

877      the Proterozoic biosphere. Nature 431, 834–838. https://doi.org/10.1038/nature02974

878 Kaljo, D., Martma, T., 2006. Application of carbon isotope stratigraphy to dating the Baltic

879      Silurian rocks. GFF 128, 123–129. https://doi.org/10.1080/11035890601282123

880 Kaljo, D., Martma, T., 2000. Carbon isotopic composition of Llandovery rocks (East Baltic

881      Silurian) with environmental interpretation, in: Proceedings of the Estonian Academy of

882      Sciences, Geology. pp. 267–283.

883 Kampschulte, A., Strauss, H., 2004. The sulfur isotopic evolution of Phanerozoic seawater based

884      on the analysis of structurally substituted sulfate in carbonates. Chem. Geol. 204, 255–286.

885      https://doi.org/10.1016/J.CHEMGEO.2003.11.013

886 Kiipli, E., Kiipli, T., Kallaste, T., 2006. Identification of the O-bentonite in the deep shelf

887      sections with implication on stratigraphy and lithofacies, East Baltic Silurian. GFF 128,

888 255–260. https://doi.org/10.1080/11035890601283255

889 Kiipli, T., Orlova, K., Kiipli, E., Kallaste, T., 2008. Use of immobile trace elements for the

890 correlation of Telychian bentonites on Saaremaa Island, Estonia, and mapping of volcanic

891 ash clouds. Est. J. Earth Sci. 57, 39–52. https://doi.org/10.3176/earth.2008.1.04

892 Kozik, N.P., Young, S.A., Bowman, C.N., Saltzman, M.R., Them, T.R., 2019. Middle–Upper

893 Ordovician (Darriwilian–Sandbian) paired carbon and sulfur isotope stratigraphy from the

894 Appalachian Basin, USA: Implications for dynamic redox conditions spanning the peak of

895 the Great Ordovician Biodiversification Event. Palaeogeogr. Palaeoclimatol. Palaeoecol.

896 520, 188–202. https://doi.org/10.1016/j.palaeo.2019.01.032

897 Kump, L.R., Arthur, M.A., 1999. Interpreting carbon-isotope excursions: carbonates and organic

898 matter. Chem. Geol. 161, 181–198. https://doi.org/10.1016/S0009-2541(99)00086-8

899 Lehnert, O., Männik, P., Joachimski, M.M., Calner, M., Frýda, J., 2010. Palaeoclimate

900 perturbations before the Sheinwoodian glaciation: A trigger for extinctions during the

901 'Ireviken Event.' Palaeogeogr. Palaeoclimatol. Palaeoecol. 296, 320–331.

902 https://doi.org/10.1016/j.palaeo.2010.01.009

903 Liu, Xi, Deng, W., Wei, G., 2019. Carbon and oxygen isotopic analyses of calcite in calcite–

904 dolomite mixtures: Optimization of selective acid extraction. Rapid Commun. Mass

905 Spectrom. 33, 411–418. https://doi.org/10.1002/rcm.8365

906 Liu, Xiting, Fike, D., Li, A., Dong, J., Xu, F., Zhuang, G., Rendle-Bühring, R., Wan, S., 2019.

907 Pyrite sulfur isotopes constrained by sedimentation rates: Evidence from sediments on the

908 East China Sea inner shelf since the late Pleistocene. Chem. Geol. 505, 66–75.

909 https://doi.org/10.1016/j.chemgeo.2018.12.014

910 Lowenstein, T.K., Hardie, L.A., Timofeeff, M.N., Demicco, R. V., 2003. Secular variation in

seawater chemistry and the origin of calcium chloride basinal brines. Geology 31, 857. https://doi.org/10.1130/G19728R.1

Loydell, D.K., Nestor, V., Mnnik, P., 2010. Integrated biostratigraphy of the lower silurian of the Kolka-54 core, Latvia. Geol. Mag. 147, 253–280. https://doi.org/10.1017/S0016756809990574

Männik, P., Põldvere, A., Nestor, V., Kallaste, T., Kiipli, T., Martma, T., 2014. The Llandovery-Wenlock boundary interval in west-central continental Estonia: an example from the Suigu (S-3) core section. Est. J. Earth Sci. 63, 1–17. https://doi.org/10.3176/earth.2014.01

Marenco, P.J., Corsetti, F.A., Hammond, D.E., Kaufman, A.J., Bottjer, D.J., 2008a. Oxidation of pyrite during extraction of carbonate associated sulfate. Chem. Geol. 247, 124–132. https://doi.org/10.1016/j.chemgeo.2007.10.006

Marenco, P.J., Corsetti, F.A., Kaufman, A.J., Bottjer, D.J., 2008b. Environmental and diagenetic variations in carbonate associated sulfate: An investigation of CAS in the Lower Triassic of the western USA. Geochim. Cosmochim. Acta 72, 1570–1582. https://doi.org/10.1016/j.gca.2007.10.033

Munnecke, A., Calner, M., Harper, D.A.T., Servais, T., 2010. Ordovician and Silurian sea–water chemistry, sea level, and climate: A synopsis. Palaeogeogr. Palaeoclimatol. Palaeoecol. 296, 389–413. https://doi.org/10.1016/j.palaeo.2010.08.001

Munnecke, A., Samtleben, C., Bickert, T., 2003. The Ireviken Event in the lower Silurian of Gotland, Sweden – relation to similar Palaeozoic and Proterozoic events. Palaeogeogr. Palaeoclimatol. Palaeoecol. 195, 99–124. https://doi.org/10.1016/S0031-0182(03)00304-3

Nestor, H., Einasto, R., 1997. Ordovician and Silurian Carbonate sedimentation basin, in: Geology and Mineral Resources of Estonia. Estonian Academy Publishers, Tallinn, pp.

934    192–204.

935    Nestor, V., 2010. Distribution of Silurian chitinozoans. Viki Drill Core. Est. Geol. Sect. Bulletin

936        1, 19–20.

937    Newton, R.J., Pevitt, E.L., Wignall, P.B., Bottrell, S.H., 2004. Large shifts in the isotopic

938        composition of seawater sulphate across the Permo-Triassic boundary in northern Italy.

939        Earth Planet. Sci. Lett. 218, 331–345. https://doi.org/10.1016/S0012-821X(03)00676-9

940    Pasquier, V., Sansjofre, P., Rabineau, M., Revillon, S., Houghton, J., Fike, D.A., 2017. Pyrite

941        sulfur isotopes reveal glacial−interglacial environmental changes. Proc. Natl. Acad. Sci.

942        114, 5941–5945. https://doi.org/10.1073/pnas.1618245114

943    Paytan, A., 1998. Sulfur Isotopic Composition of Cenozoic Seawater Sulfate. Science (80-. ).

944        282, 1459–1462. https://doi.org/10.1126/science.282.5393.1459

945    Percak-Dennett, E., He, S., Converse, B., Konishi, H., Xu, H., Corcoran, A., Noguera, D., Chan,

946        C., Bhattacharyya, A., Borch, T., Boyd, E., Roden, E.E., 2017. Microbial acceleration of

947        aerobic pyrite oxidation at circumneutral pH. Geobiology 15, 690–703.

948        https://doi.org/10.1111/gbi.12241

949    Present, T.M., 2018. Controls on the Sulfur Isotopic Composition of Carbonate-Associated

950        Sulfate. California Institute of Technology.

951    Present, T.M., Adkins, J.F., Fischer, W.W., 2020. Variability in Sulfur Isotope Records of

952        Phanerozoic Seawater Sulfate. Geophys. Res. Lett. 47.

953        https://doi.org/10.1029/2020GL088766

954    Present, T.M., Gutierrez, M., Paris, G., Kerans, C., Grotzinger, J.P., Adkins, J.F., 2019.

955        Diagenetic controls on the isotopic composition of carbonate-associated sulphate in the

956        Permian Capitan Reef Complex, West Texas. Sedimentology 66, 2605–2626.

957         https://doi.org/10.1111/sed.12615

958   Present, T.M., Paris, G., Burke, A., Fischer, W.W., Adkins, J.F., 2015. Large Carbonate

959         Associated Sulfate isotopic variability between brachiopods, micrite, and other sedimentary

960         components in Late Ordovician strata. Earth Planet. Sci. Lett. 432, 187–198.

961         https://doi.org/10.1016/J.EPSL.2015.10.005

962   Rennie, V.C.F., Turchyn, A. V., 2014. The preservation of $\delta SSO434$ and $\delta OSO418$ in carbonate-

963         associated sulfate during marine diagenesis: A 25 Myr test case using marine sediments.

964         Earth Planet. Sci. Lett. 395, 13–23. https://doi.org/10.1016/J.EPSL.2014.03.025

965   Richardson, J.A., Keating, C., Lepland, A., Hints, O., Bradley, A.S., Fike, D.A., 2019a. Silurian

966         records of carbon and sulfur cycling from Estonia: The importance of depositional

967         environment on isotopic trends. Earth Planet. Sci. Lett. 512, 71–82.

968         https://doi.org/10.1016/j.epsl.2019.01.055

969   Richardson, J.A., Newville, M., Lanzirotti, A., Webb, S.M., Rose, C. V, Catalano, J.G., Fike,

970         D.A., 2019b. Depositional and Diagenetic Constrains on the Abundance and Spatial

971         Variability of Carbonate-Associated Sulfate. Chem. Geol. 523, 59–72.

972         https://doi.org/10.1016/J.CHEMGEO.2019.05.036

973   Rose, C. V., Fischer, W.W., Finnegan, S., Fike, D.A., 2019. Records of carbon and sulfur

974         cycling during the Silurian Ireviken Event in Gotland, Sweden. Geochim. Cosmochim. Acta

975         246, 299–316. https://doi.org/10.1016/j.gca.2018.11.030

976   Rubel, M., Hints, O., Meidla, T., Nestor, V., Sarv, L., Sibul, I., 2007. Lower Silurian

977         biostratigraphy of the Viirelaid core, western Estonia. Est. J. Earth Sci. 56, 193–204.

978         https://doi.org/10.3176/earth.2007.01

979   Samtleben, C., Munnecke, A., Bickert, T., 2000. Development of facies and C/O-isotopes in

980      transects through the Ludlow of Gotland: Evidence for global and local influences on a

981      shallow-marine environment. Facies 43, 1–38. https://doi.org/10.1007/BF02536983

982 Sim, M.S., Bosak, T., Ono, S., 2011. Large sulfur isotope fractionation does not require

983      disproportionation. Science (80-. ). 333, 74–77. https://doi.org/10.1126/science.1205103

984 Stebbins, A., Algeo, T.J., Olsen, C., Sano, H., Rowe, H., Hannigan, R., 2018. Sulfur-isotope

985      evidence for recovery of seawater sulfate concentrations from a PTB minimum by the

986      Smithian-Spathian transition. Earth-Science Rev.

987      https://doi.org/10.1016/J.EARSCIREV.2018.08.010

988 Strauss, H., 1997. The isotopic composition of sedimentary sulfur through time. Palaeogeogr.

989      Palaeoclimatol. Palaeoecol. 132, 97–118. https://doi.org/10.1016/S0031-0182(97)00067-9

990 Swart, P.K., 2015. The geochemistry of carbonate diagenesis: The past, present and future.

991      Sedimentology 62, 1233–1304. https://doi.org/10.1111/sed.12205

992 Swart, P.K., Eberli, G., 2005. The nature of the $\delta 13C$ of periplatform sediments: Implications for

993      stratigraphy and the global carbon cycle. Sediment. Geol. 175, 115–129.

994      https://doi.org/10.1016/J.SEDGEO.2004.12.029

995 Thompson, C.K., Kah, L.C., 2012. Sulfur isotope evidence for widespread euxinia and a

996      fluctuating oxycline in Early to Middle Ordovician greenhouse oceans. Palaeogeogr.

997      Palaeoclimatol. Palaeoecol. 313–314, 189–214.

998      https://doi.org/10.1016/J.PALAEO.2011.10.020

999 Tonarová, P., Hints, O., Eriksson, M.E., 2014. Impact of the Silurian Ireviken Event on

1000      polychaete faunas: New insights from the Viki drill core, western Estonia. GFF 136, 270–

1001      274. https://doi.org/10.1080/11035897.2013.862855

1002 Torsvik, T.H., Cocks, L.R.M., 2013. New global palaeogeographical reconstructions for the

Early Palaeozoic and their generation. Geol. Soc. Mem. 38, 5–24.

https://doi.org/10.1144/M38.2

Tostevin, R., He, T., Turchyn, A. V., Wood, R.A., Penny, A.M., Bowyer, F., Antler, G., Shields, G.A., 2017. Constraints on the late Ediacaran sulfur cycle from carbonate associated sulfate. Precambrian Res. 290, 113–125. https://doi.org/10.1016/j.precamres.2017.01.004

Trotter, J.A., Williams, I.S., Barnes, C.R., Männik, P., Simpson, A., 2016. New conodont $\delta18O$ records of Silurian climate change: Implications for environmental and biological events. Palaeogeogr. Palaeoclimatol. Palaeoecol. 443, 34–48. https://doi.org/10.1016/j.palaeo.2015.11.011

Turchyn, A. V., Schrag, D.P., 2006. Cenozoic evolution of the sulfur cycle: Insight from oxygen isotopes in marine sulfate. Earth Planet. Sci. Lett. 241, 763–779. https://doi.org/10.1016/J.EPSL.2005.11.007

Turchyn, A. V., Schrag, D.P., Coccioni, R., Montanari, A., 2009. Stable isotope analysis of the Cretaceous sulfur cycle. Earth Planet. Sci. Lett. 285, 115–123. https://doi.org/10.1016/J.EPSL.2009.06.002

Vandenbroucke, T.R.A., Munnecke, A., Leng, M.J., Bickert, T., Hints, O., Gelsthorpe, D., Maier, G., Servais, T., 2013. Reconstructing the environmental conditions around the Silurian Ireviken Event using the carbon isotope composition of bulk and palynomorph organic matter. Geochemistry, Geophys. Geosystems 14, 86–101. https://doi.org/10.1029/2012GC004348

Xiao, S., Cui, H., Kang, J., McFadden, K.A., Kaufman, A.J., Kitajima, K., Fournelle, J.H., Schwid, M., Nolan, M., Baele, J.-M., Valley, J.W., 2020. Using SIMS to decode noisy stratigraphic $\delta13C$ variations in Ediacaran carbonates. Precambrian Res. 105686.

1026    https://doi.org/10.1016/j.precamres.2020.105686

1027  Young, S.A., Benayoun, E., Kozik, N.P., Hints, O., Martma, T., Bergström, S.M., Owens, J.D.,

1028    2020. Marine redox variability from Baltica during extinction events in the latest

1029    Ordovician–early Silurian. Palaeogeogr. Palaeoclimatol. Palaeoecol. 554.

1030    https://doi.org/10.1016/j.palaeo.2020.109792

1031  Young, S.A., Gill, B.C., Edwards, C.T., Saltzman, M.R., Leslie, S.A., 2016. Middle–Late

1032    Ordovician (Darriwilian–Sandbian) decoupling of global sulfur and carbon cycles: Isotopic

1033    evidence from eastern and southern Laurentia. Palaeogeogr. Palaeoclimatol. Palaeoecol.

1034    458, 118–132. https://doi.org/10.1016/j.palaeo.2015.09.040

1035  Young, S.A., Kleinberg, A., Owens, J.D., 2019. Geochemical evidence for expansion of marine

1036    euxinia during an early Silurian (Llandovery–Wenlock boundary) mass extinction. Earth

1037    Planet. Sci. Lett. 513, 187–196. https://doi.org/10.1016/j.epsl.2019.02.023

1038

1039  **Tables**

1040  Table 1 – average $\delta^{34}S_{CAS}$ and $\delta^{34}S_{pyr}$ values and average sample-to-sample $\delta^{34}S_{CAS}$ and $\delta^{34}S_{pyr}$

1041  values for each formation to assess the variability of sulfur isotope values within a given

1042  depositional environment. The number of samples is included beside each formation name.

1043  Average sample-to-sample $\delta^{34}S_{pyr}$ is particularly high in the Velise Fm., as this includes an aberrant

1044  sample at 74.24 m of -32.38‰. Excluding this sample brings the average sample-to-sample $\delta^{34}S_{pyr}$

1045  down to 8.3‰ in the Velise Fm (given in parentheses). Similarly, the average sample-to-sample

1046  $\delta^{34}S_{pyr}$ decreases from 7 to 4.2‰ in the Jaani Formation when excluding samples that belong to

1047  the oolite (which is a rapid shallowing environment; again in parentheses).

1048

1049  **Figures**
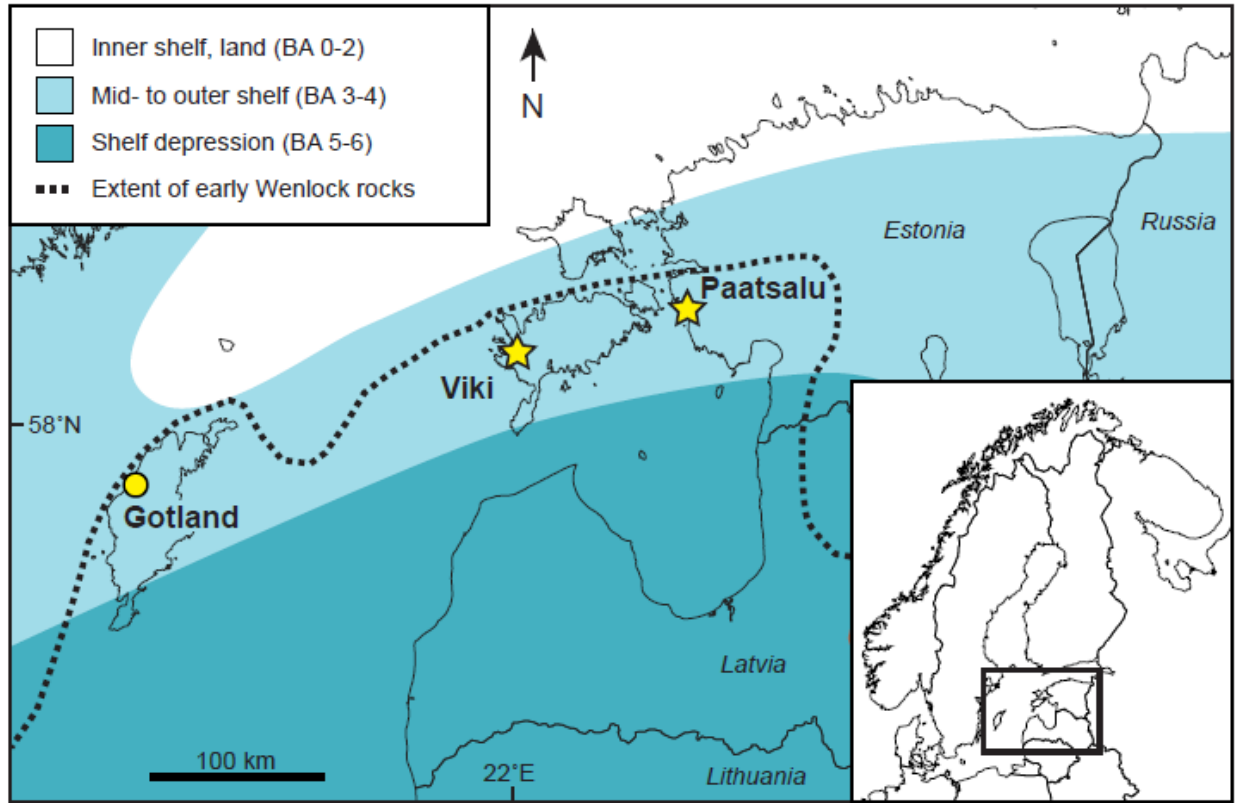
Figure 1 – Map showing the locations of Paatsalu (this study) and Viki drill cores (Richardson et al., 2019a) in Estonia (stars), and a time-equivalent comparison from Gotland Island, Sweden (Rose et al., 2019) (circle). Generalized paleogeography is shown for the early Wenlock (Baarli et al., 2003; Nestor and Einasto, 1997). BA = depth related benthic assemblages (Brett et al., 1993)
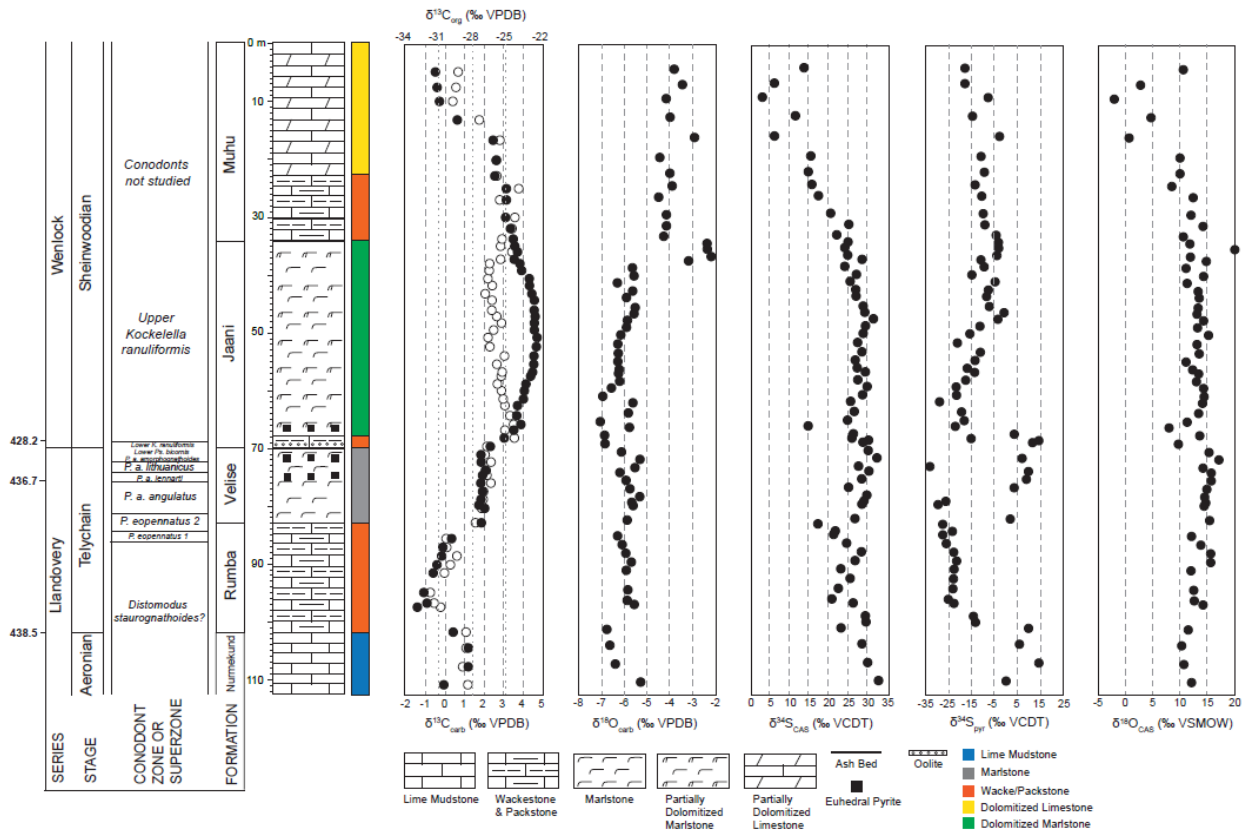
1055

Figure 2 – Paatsalu drill core stratigraphy (left) and coeval isotope chemostratigraphy. From left to right: $\delta^{13}C_{carb}$ (solid circles; dashed lines) and $\delta^{13}C_{org}$ (open circles; dotted lines), $\delta^{18}O_{carb}$, $\delta^{34}S_{CAS}$, $\delta^{34}S_{pyr}$ and $\delta^{18}O_{CAS}$. Note that the same lithofacies color coding is used in subsequent figures.
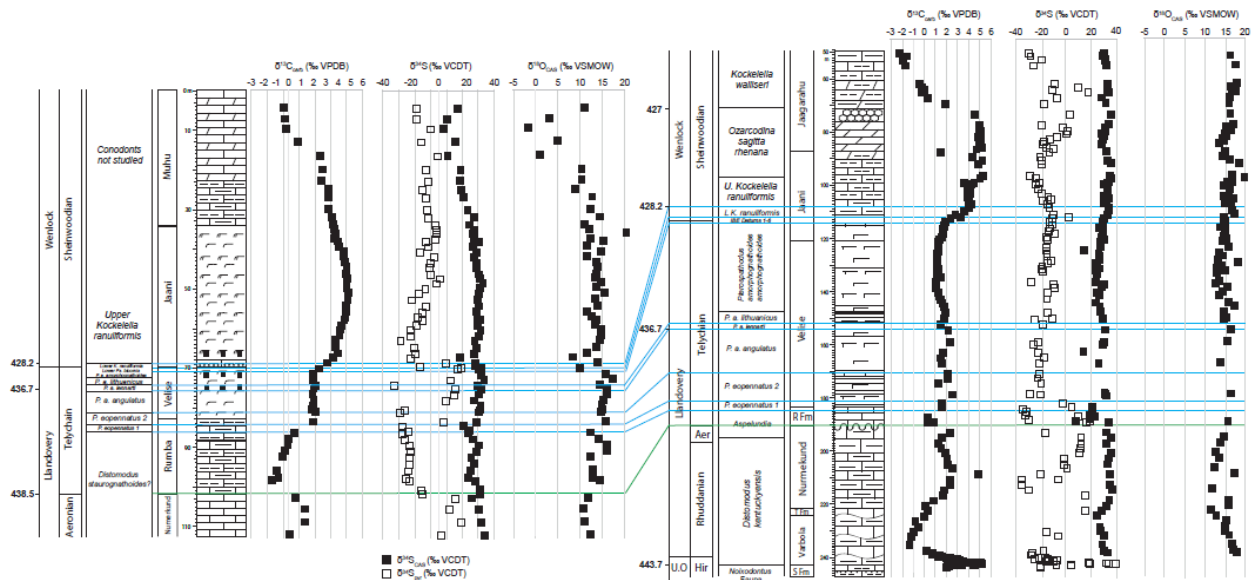
1060

Figure 3 – Comparison of $\delta^{13}C_{carb}$, $\delta^{34}S_{pyr}$, $\delta^{34}S_{CAS}$ (solid squares) and $\delta^{18}O_{CAS}$ (open squares) from Paatsalu (left) and Viki (right; Richardson et al., 2019). Correlations made based on conodont biozones (blue lines) and the top of the *Conochitina alargada* chitinozoan biozone (green line). See Fig. 2 for lithology legend.
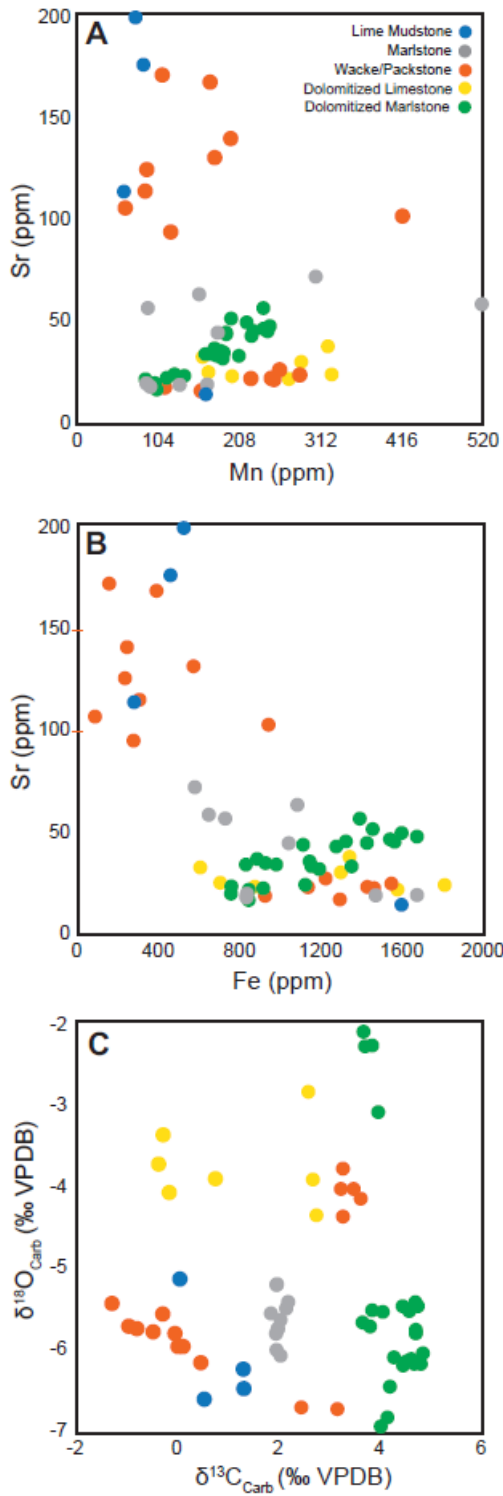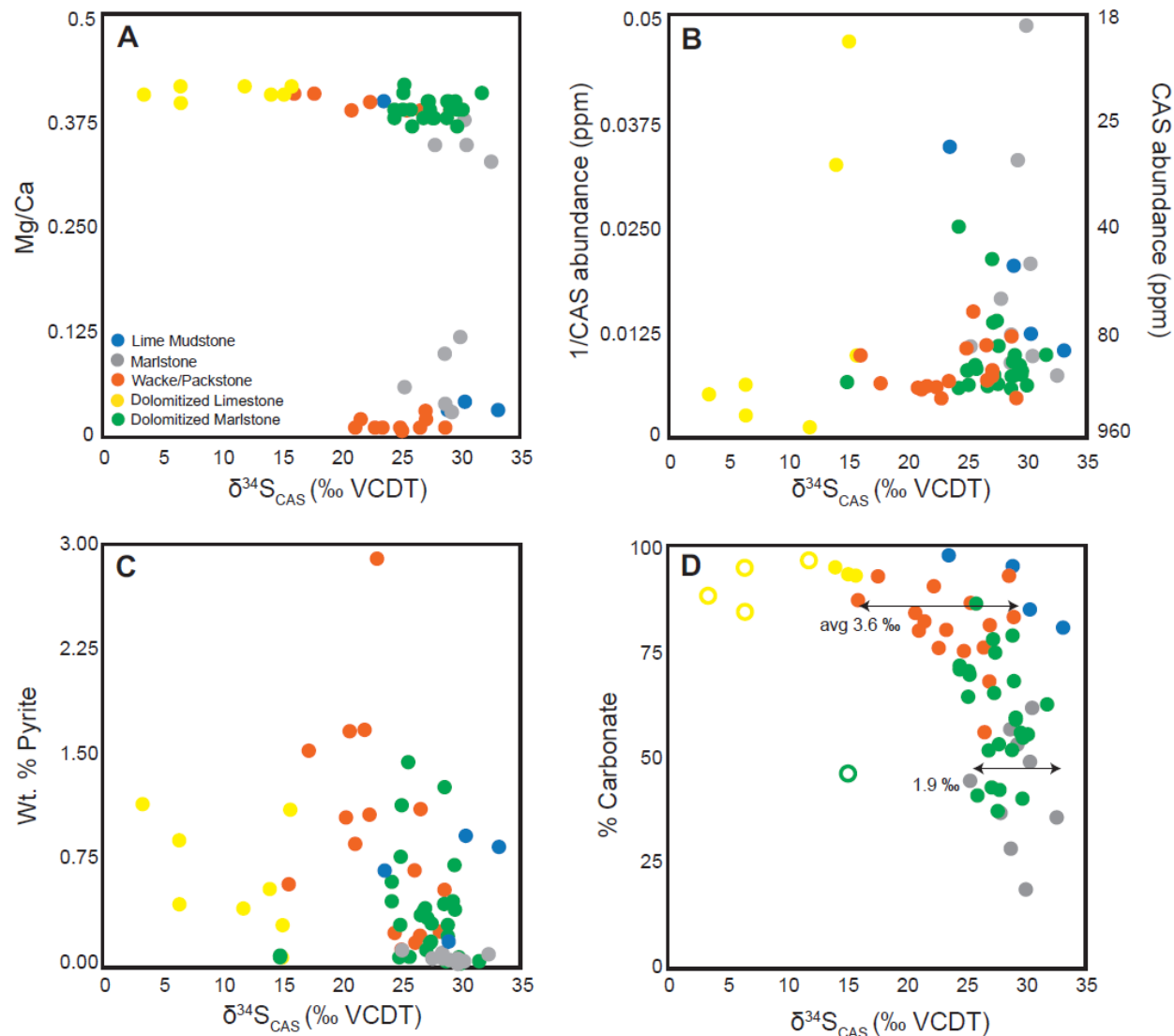
1065

Figure 4 – Cross plots of indicators of post-depositional late-stage diagenesis color-coded by

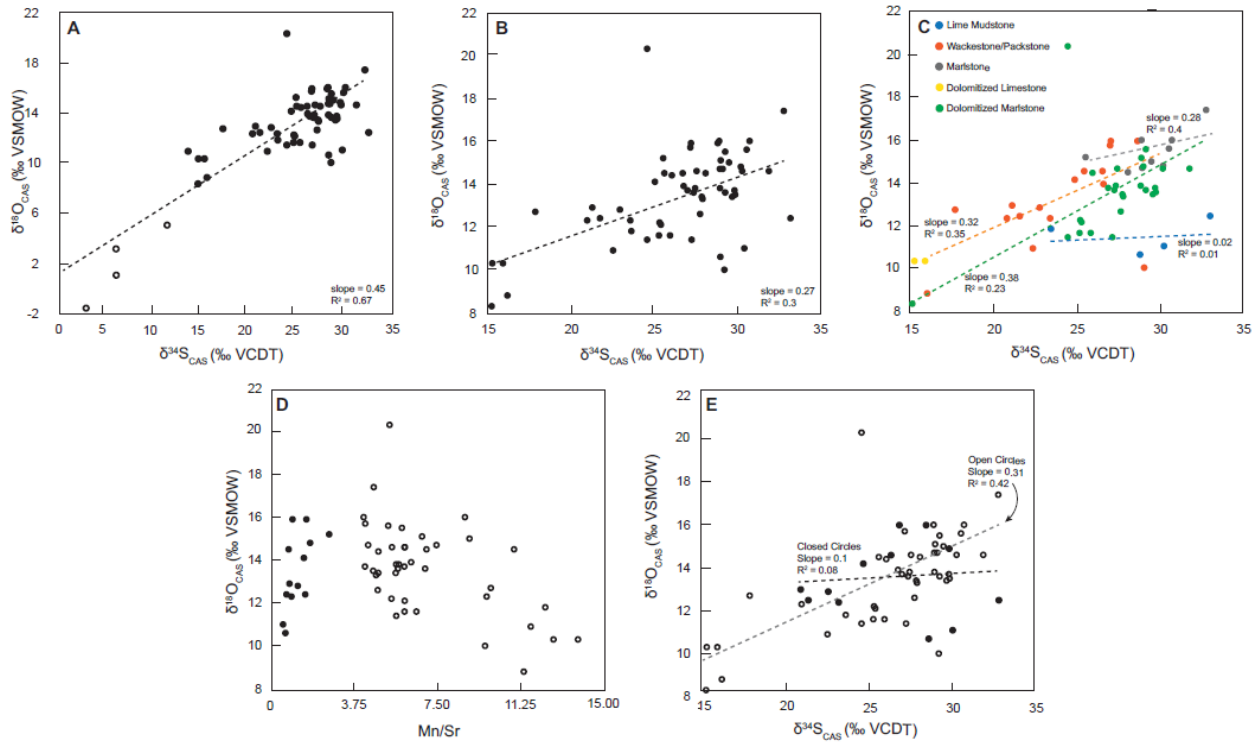lithology. (A) Sr vs. Mn abundance, (B) Sr vs. Fe abundance, (C) $\delta^{13}C_{carb}$ vs. $\delta^{18}O_{carb}$,

1068

Figure 5 – Cross plots of $\delta^{34}S_{CAS}$ vs. (A) Mg/Ca molar ratio, (B) 1/CAS abundance, (C) wt % S in pyrite and (D) carbonate abundance. Open symbols are samples thought to be altered. Arrows represent the average sample-to-sample variability in shallow-water (3.6‰) and deep-water (1.9‰) facies.

Figure 6 – Cross plots of $\delta^{18}O_{CAS}$ from the Paatsalu drill core vs. (A) $\delta^{34}S_{CAS}$ with altered samples as open circles, (B) $\delta^{34}S_{CAS}$ with altered samples shown in A removed, (C) $\delta^{34}S_{CAS}$ color-coded with lithologic information. The slope for dolomitized limestone is omitted due to the small number of samples from this unit (n = 2) (D) Mn/Sr. Open circles are samples with Mn/Sr > 4 and solid circles are samples with Mn/Sr < 4. (E) $\delta^{34}S_{CAS}$ plotted as Mn/Sr > 4 (open circles, grey dashed line) and Mn/Sr < 4 (solid circles, black dashed line).
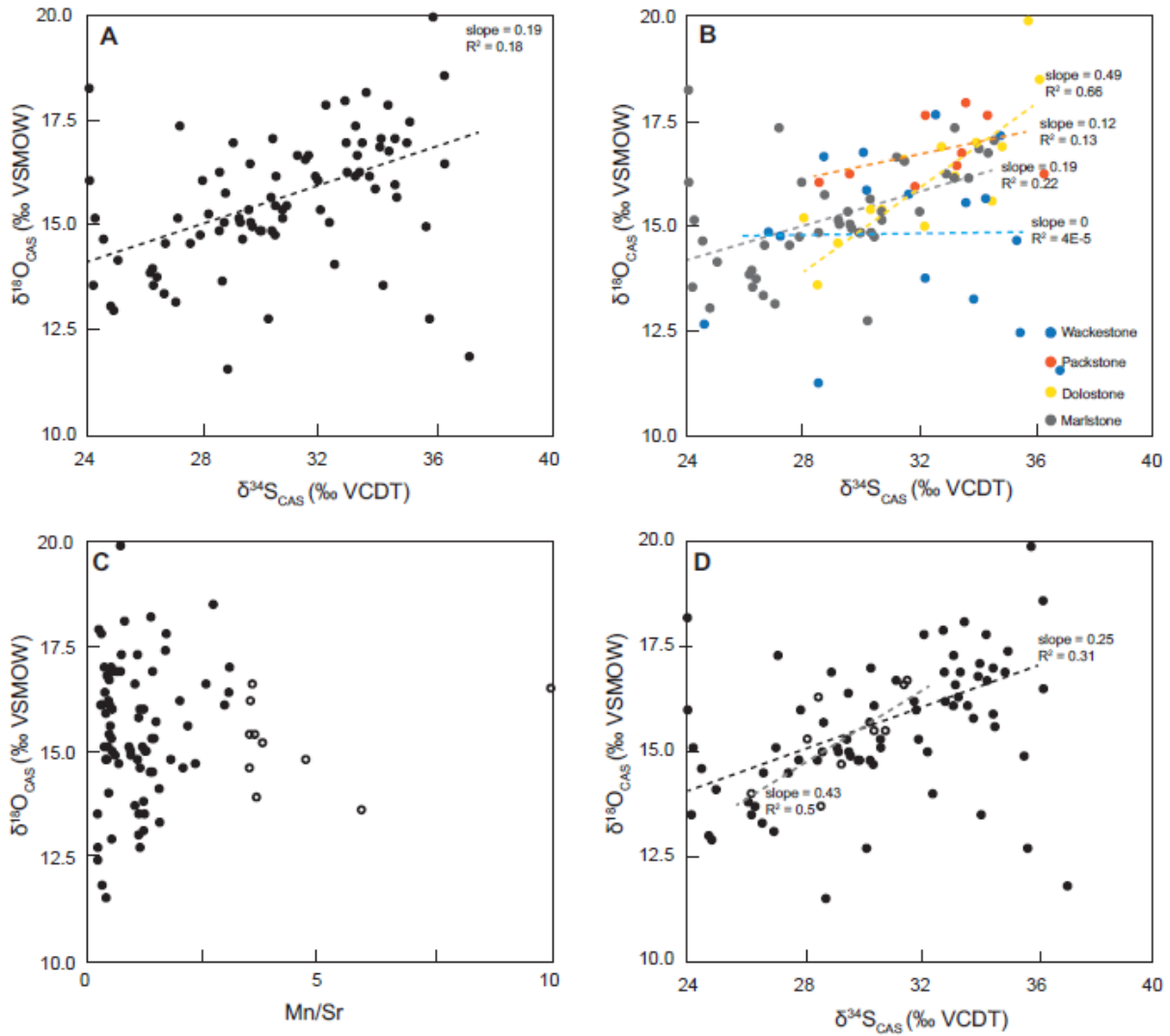
1080

1081      Figure 7 - Cross plots of $\delta^{18}O_{CAS}$ from the Viki drill core vs. (A) $\delta^{34}S_{CAS}$, (B) $\delta^{34}S_{CAS}$ color-coded

1082      with lithologic information, (C) Mn/Sr. Open circles are samples with an Mn/Sr > 4 and solid

1083      circles are samples with Mn/Sr < 4. (D) $\delta^{34}S_{CAS}$ plotted as Mn/Sr > 4 (open circles) and Mn/Sr <

1084      4 (solid circles).

1085
1086